Unsteady three-dimensional theoretical model and numerical simulation of a 120-kW chemical looping combustion pilot plant

Ziad Hamidouche [a], Enrica Masi [a,*], Pascal Fede [a], Olivier Simonin [a], Karl Mayer [b], Stefan Penthor [b]

[a] Institut de Mécanique des Fluides de Toulouse (IMFT), Université de Toulouse, CNRS, INPT, UPS, Toulouse, France
[b] Vienna University of Technology, Institute of Chemical Engineering, Getreidemarkt 9/166, 1060 Vienna, Austria

HIGHLIGHTS

- An Euler Euler model for the two phase flow (solid OC and gas fuel) is developed.
- 3D unsteady numerical simulations of a CLC unit based on a DCFB are performed.
- Good agreement between numerical results and experimental measurements is found.
- Numerical results prove the ability of the approach to predict the CLC process.
- The local and instantaneous CLC behavior is analyzed and discussed.

GRAPHICAL ABSTRACT

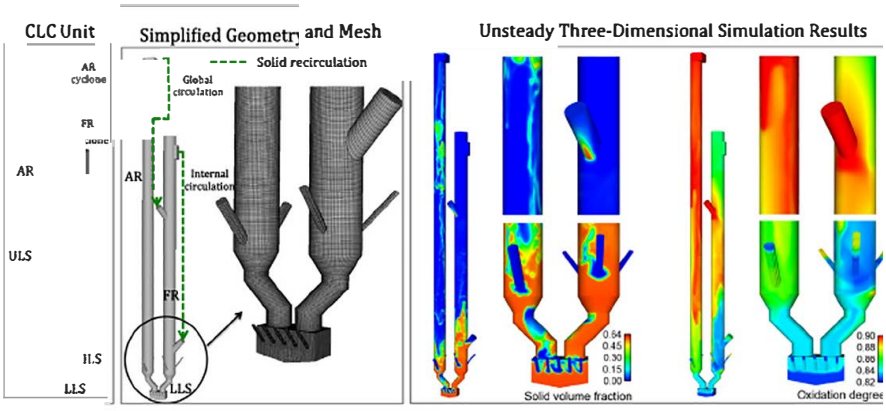

ABSTRACT

In this paper, reactive unsteady three dimensional numerical simulations of a chemical looping combustion (CLC) unit are presented. The configuration is a 120 kW pilot plant working with perovskite, $CaMn_{0.9}Mg_{0.1}O_{3-\delta}$, as the selected oxygen carrier. Numerical simulations were performed using NEPTUNE_CFD code in the frame of an Euler Euler approach by computing both gas and solid phases in an Eulerian technique, accounting for specific closures in order to model the interphase mass, and momentum and energy transfers. Heterogeneous reduction and oxidation (gas solid) reactions were modeled by means of a grain model to account for the competing mechanisms of the chemical reaction onto the grain surface, the gaseous diffusion through the product layer around the grain, and the external transfer through the gas mixture surrounding the particle. Results from numerical simulations were assessed against experimental measurements and analyzed in order to acquire insight on the local behavior of reactive gas particle flow in the CLC system. The theoretical/numerical tool developed in this work can be used for the design upgrade of crucial parts of the system in the stage of scaling up from pilot to industrial plants.

Keywords:
Chemical looping combustion
Fluidized beds
Gas–solid reactions
3D CFD

1. Introduction

Chemical looping combustion (CLC) is a process based on the combustion of fuel with the oxygen supplied by a solid material, called an oxygen carrier (OC). This technique, generally based on a dual circulation fluidized bed (Pröll et al., 2009a), involves the

* Corresponding author.
E-mail address: enrica.masi@imft.fr (E. Masi).

circulation of the oxygen carrier between two reactors: a fuel reactor (FR) for fuel combustion and an air reactor (AR) for OC regeneration. In the fuel reactor, a reduction reaction in solid OC by the gaseous fuel occurs, in which compositions can be expressed as MeO_x and C_nH_{2m}. The reduction reaction mainly produces CO_2 and H_2O in the flue gas and converts the oxygen carrier to its reduced form, $MeO_{x\ 1}$ (Eq. (1)). After the condensation of water vapor, CO_2 is cooled and pressurized in stages to yield liquid CO_2 ready for storage. According to the CLC operating mode, the reduced material ($MeO_{x\ 1}$) is sent back to the air reactor and regenerated by air according to an oxidation reaction (Eq. (2)). The redox cycle may be summarized as follows:

$$(2n+m)\mathrm{MeO_x\ (s)} + \mathrm{C_nH_{2m}} \rightarrow (2n+m)\mathrm{MeO_{x\ 1}\ (s)} + n\mathrm{CO_2} + m\mathrm{H_2O} \quad (1)$$

$$(2n+m)\mathrm{MeO_{x\ 1}\ (s)} + (n+m/2)\mathrm{O_2} \rightarrow (2n+m)\mathrm{MeO_x\ (s)}, \quad (2)$$

where n and m are appropriate stoichiometric coefficients, s indicates a solid species, and MeO_x states for metal oxide. Whereas the oxidation reaction (Eq. (2)) is always an exothermic process associated with heat release, the reduction reaction may be an endothermic or a slightly exothermic reaction, depending on OC and the fuel employed in the CLC system. When the reduction is an endothermic reaction, the heat required is provided by the solid oxygen carrier, which maintains the temperature of the two reactors practically constant, as the carrier circulates in the system. The overall chemical reaction and corresponding heat release in the two reactors in the CLC system are the same as in conventional combustion, where fuel is directly burned by air, but with the advantage that combustion occurs without CO_2 emission into the atmosphere. This combustion is given by the following:

$$\mathrm{C_nH_{2m}} + (n+m/2)\mathrm{O_2} \rightarrow n\mathrm{CO_2} + m\mathrm{H_2O}. \quad (3)$$

The chemical looping combustion technology has exhibited a unique potential in reducing energy and cost penalty for CO_2 capture (Gauthier et al., 2017). Currently, research efforts are focused on the selection of an appropriate, efficient, environment friendly, and low cost oxygen carrier and related manufacturing techniques (e.g., see the seventh framework program (FP7) project SUCCESS (Penthor et al., 2017) (Scale Up of oxygen Carrier for Chemical looping combustion using Environmentally Sustainable materials). These are aimed at defining OC and production techniques for their use on an industrial scale (Hallberg et al., 2014; Cabello et al., 2014; Pishahang et al., 2016; Cabello et al., 2016a; Cabello et al., 2016b; Jing et al., 2016)). Moreover, scaling up from pilot to industrial facilities requires designing and sizing industrial plants while defining commercial benefits and costs.

In the laboratory, cold flow models are widely used to study the hydrodynamics of CLC units with the goal of understanding and improving operating conditions (Markström and Lyngfelt, 2012; Penthor et al., 2016). Thereafter, designing and sizing are performed by using engineering tools and providing global quantities by balance investigations and process models (Bolhàr Nordenkampf et al., 2009; Marx et al., 2013; Ohlemüller et al., 2015; Zerobin et al., 2016; Zerobin et al., 2017; Haus et al., 2017). In order to model the CLC process and predict the CLC behavior, a one or one half dimensional model is employed because of its considerably low computational cost and previous successful results (Abad et al., 2010; Abad et al., 2013; García Labiano et al., 2013; Abad et al., 2014; Abad et al., 2018). On the other hand, unsteady two and three dimensional modeling are useful approaches in computational fluid dynamics (CFD) to understand and predict local and instantaneous CLC behaviors, particularly when it is necessary to analyze and improve crucial parts of the CLC unit without having to resort to considerably expensive laboratory experiments. Certainly, the use of CFD makes it possible to characterize the local behavior of the CLC system, and therefore, provides useful information for scaling up from the laboratory to the industrial scale.

Most reactive studies that employ CFD (for example, see two dimensional (Deng et al., 2008; Jung and Gamwo, 2008; Mahalatkar et al., 2011a) or three dimensional (Chen et al., 2017; Alobaid et al., 2015; Sharma et al., 2017) studies) focus on the fuel reactor behavior, because it is considered a crucial part of the CLC process, especially when solid fuel is used. Concerning reactive CLC systems based on interconnected or dual circulation fluidized beds (DCFB), several two dimensional unsteady numerical simulations are also reported in the literature. Examples on these are the works of Kruggel Emden et al. (2010) and Zhang et al. (2017), who simulated both AR and FR separately while modeling their coupling by inlet/outlet boundary conditions. Other examples include the works of Mahalatkar et al. (2011b) and Wang et al. (2014), who performed numerical simulations of interconnected reactive CLC systems at small and pilot scales, respectively. These works on DCFB were conducted using an Euler Euler approach on fueled gas systems. Another example is the study of Su et al. (2015) who performed two dimensional numerical simulations of a DCFB CLC using coal as fuel. On the other hand, a small number of studies based on a three dimensional model of a DCFB CLC unit may be found in the literature. Guan et al. (2014, 2016) conducted three dimensional (3D) numerical simulations of a cold flow model, scaled from a 30 MW model by Johansson et al. (2003), and studied the effects of drag correlation on the predictions and operating conditions on the solid circulation rate. Geng et al. (2015) used the 3D CFD for reproducing a 120 kW cold flow model of Pröll et al. (2009b) and studied the effects of fluidization rate on the solid circulation. In these works, results were compared with experimental measurements of the gas pressure drop; however, the reactions were not taken into account. Banerjee and Agarwal (2015) performed two dimensional (2D) and 3D numerical simulations of a small scale 300 W reactive CLC unit (Abad et al. (2007)), and a comparison of their results identified the ability of 3D modeling to improve predictions. Comparisons with experiments were conducted by assessing the species mass fractions at the FR outlet. Parker (2014), performed 3D numerical simulations of a CLC system, using coal as fuel by means of the Euler Lagrange method, and numerical results were compared with expected (target) values.

Because of the scarcity of reports in literature on unsteady three dimensional simulations of DCFB CLC systems and their comparisons with experimental results, reactive three dimensional modeling and related applications represent a current topic of research. Accordingly, in this present study, an Euler Euler approach, accounting for reactions, was developed with the goal of providing a theoretical and numerical tool for CLC modeling and design upgrade for its use on an industrial scale. The results obtained from 3D unsteady numerical simulations were then assessed against experimental measurements over all quantities inherent in the CLC process, available from experiments. Numerical results were finally analyzed in order to gain insight on the CLC process. The present paper is organized as follows. In Section 2, the experiment of reference, previously conducted at TU Wien (Mayer et al., 2015), is briefly recalled and selected operating point is described. The Euler Euler model developed in this study is detailed in Section 3. In Section 4, numerical simulations are presented, and their results are discussed in Section 5. Finally, conclusions are offered in Section 6.

2. Description of the experimental setup

The pilot plant is a 120 kW CLC unit operating at the Vienna University of Technology (TU Wien). It is conceived as a dual

circulation fluidized bed composed of an air reactor and a fuel reactor connected to each other by upper and lower loop seals (Kolbitsch et al., 2009a; Mayer et al., 2015). The loop seals are fluidized by steam to avoid the mixture of gas between the two reactors. Solid circulation is made possible because of the fluidization in the reactors, by air or fuel, depending on the reactor, and by steam coming from the lower loop seal (LLS). In the experiments, natural gas was used as the fluidizing gas in FR. Internal circulation of solid may occur in the fuel reactor because of a fluidized by steam loop seal (internal loop seal). The fuel reactor was insulated, whereas the air reactor was equipped with two cooling jackets. The cooling medium was steam and/or air. A sketch of the experimental pilot is given in Fig. 1, and main dimensions are listed in Table 1. Additional details may be found in Mayer et al. (2015). In the experiments, different oxygen carriers, each at two different operating points, were investigated. In the numerical simulations, only one oxygen carrier at one operating point was used. The oxygen carrier was the perovskite $CaMn_{0.9}Mg_{0.1}O_{3-\delta}$ (also referred to as C14), whose main physical properties are summarized in Table 2. The set of parameters corresponding to the selected operating point are summarized in Tables 3–5. Experimental data were used as inputs for numerical simulations, and experimental measurements were retained for the purpose of comparison.

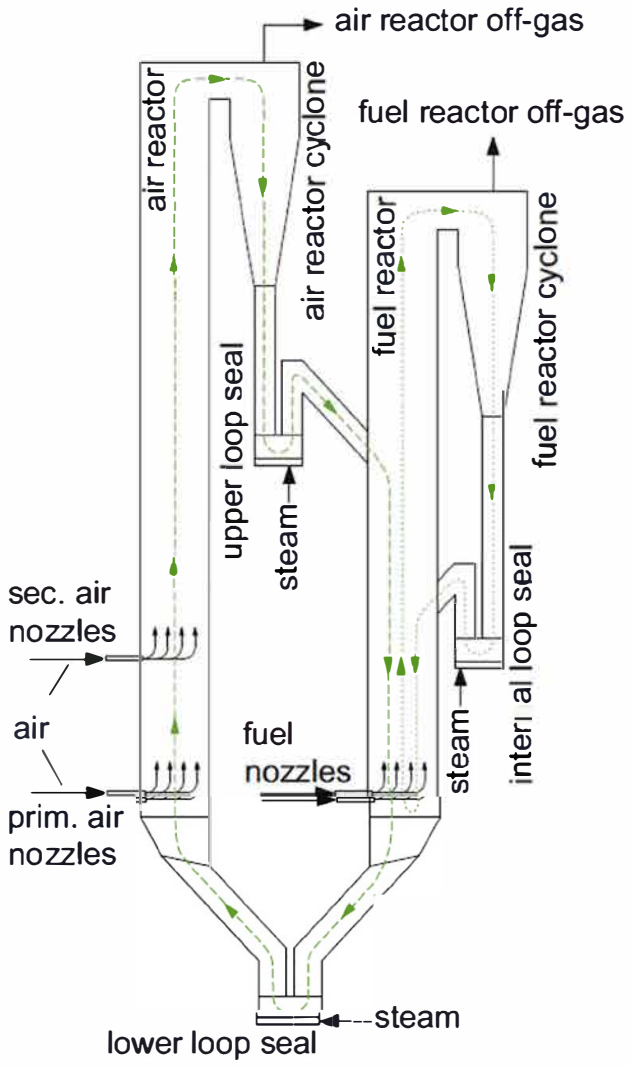

Fig. 1. Experimental CLC unit scheme, excerpted from Mayer et al. (2015).

Table 1
Main dimensions of TU Wien CLC unit.

	AR	FR
Inner diameter	150 mm	159.3 mm
Reactor height	4 m	3 m

Table 2
Main properties of C14.

C14 oxygen carrier	
Particle mean diameter	130 μm
Bulk density	1542 kg m^{-3}
Particle density	3200 kg m^{-3}

Table 3
Solid inventories.

Bed material	(kg)
Total inventory	55
FR active inventory	13.5
AR active inventory	6.5

Table 4
Gas feed to reactors.

FR	
CH_4	7.34 Nm^3 h^{-1}
Other C_xH_y	0.15 Nm^3 h^{-1}
N_2	0.08 Nm^3 h^{-1}
CO_2	0.02 Nm^3 h^{-1}
Total	7.59 Nm^3 h^{-1}
Temperature	1223 K
AR	
Air	90.78 Nm^3 h^{-1}
Temperature	1203 K

Table 5
Fluidizing steam to the loop seals.

Fluidizing steam	
Upper loop seal (ULS)	3 kg h^{-1}
Lower loop seal (LLS)	2 kg h^{-1}
Internal loop seal (ILS)	2 kg h^{-1}
Temperature	453 K

3. Modeling approach

An Euler Euler approach (Simonin, 2000; Boëlle et al., 1995; Gobin et al., 2003) (also known as a two fluid model) is used to model and predict interactions between the reactive particulate phase and gas mixture composed of N chemical species. Such an approach relies on the solution of two separate systems (one for each phase), including mass, momentum, and enthalpy transport equations. Additional equations are needed to predict the gaseous species evolution and gas density changes for the gas phase, and solid conversions for the particulate phase. The two systems of equations are coupled by specific closure modeling interphase mass, momentum, and energy transfers.

3.1. Mass, momentum, and enthalpy transport equations

The system of equations describing the evolution of mass, momentum, and enthalpy quantities is written, for each phase, as follows:

$$\frac{\partial}{\partial t}(\alpha_k\rho_k) + \frac{\partial}{\partial x_j}(\alpha_k\rho_k U_{k,j}) \quad \Gamma_k \tag{4}$$

$$\alpha_k\rho_k\left(\frac{\partial U_{k,i}}{\partial t} + U_{k,j}\frac{\partial U_{k,i}}{\partial x_j}\right) \quad \alpha_k\frac{\partial P_g}{\partial x_i} + \alpha_k\rho_k g_i + I_{k'\to k,i} + [U_{\sigma,i} \quad U_{k,i}]\Gamma_k \quad \frac{\partial \Sigma_{k,ij}}{\partial x_j} \tag{5}$$

$$\alpha_k\rho_k\left(\frac{\partial H_k}{\partial t} + U_{k,j}\frac{\partial H_k}{\partial x_j}\right) \quad \frac{\partial}{\partial x_j}\left(\alpha_k\rho_k K_k^{eff}\frac{\partial H_k}{\partial x_j}\right) + [H_\sigma \quad H_k]\Gamma_k + \Pi_{k'\to k}. \tag{6}$$

In the above equations, α_k represents the volume fraction of the phase k, which may either be the gas (k g) or particulate phase (k p); ρ_k and $U_{k,j}$ are the phase density and velocity, respectively; H_k is the phase mass enthalpy and Γ_k represents the interphase mass transfer rate per unit volume, which satisfies the condition $\sum_k \Gamma_k$ $\Gamma_g + \Gamma_p$ 0; $U_{\sigma,i}$ and H_σ are the velocity and mass enthalpy of the mass flux crossing the particle surface, respectively, because of the reaction between solid OC and the gaseous phase; $I_{k'\to k,i}$ and $\Pi_{k'\to k}$ account for the interphase (gas solid) momentum and energy transfer, respectively, because of local perturbations induced by the particle, where, in both these terms, k' represents the phase other than k, therefore denoting the effects of the phase k' on the phase k; $\Sigma_{k,ij}$ is the sum of the viscous and turbulent stress tensors for the gas, or the particle kinetic and collisional stress tensors for the solid; K_k^{eff} represents an effective thermal diffusivity accounting for turbulent and laminar contributions for the gas. For the particulate phase, this term accounts for the mass enthalpy transport by velocity fluctuations and radiative transfer within the solid phase. Details concerning the closure of $I_{k'\to k,i}$ and $\Sigma_{k,ij}$ may be found in Boëlle et al. (1995) and Gobin et al. (2003), whereas the modeling of $\Pi_{k'\to k}$ and K_k^{eff} are given, for example, in Konan et al. (2010a,b). A detailed description of the Euler Euler approach used in the present study may be found in Hamidouche et al. (2018).

3.2. Evolution of particle properties

In this work, two reactions (one for the reduction and another for the oxidation) were considered for modeling the redox cycle of the perovskite oxygen carrier. Kinetic parameters and reaction mechanisms were obtained from the work of de Diego et al. (2014). In the numerical simulations, the δ parameter in the perovskite formula, $CaMn_{0.9}Mg_{0.1}O_{3\ \delta}$, was assumed to be constant. Its value was set to 0.1, despite its dependency on the temperature and oxygen partial pressure (for more details, the reader is referred to references (Bakken et al., 2005; de Diego et al., 2014; Leonidova et al., 2011)). Under such assumptions, the CLC process is described by the following reactions:

$$CaMn_{0.9}Mg_{0.1}O_{2.9} + a/2CH_4 \rightarrow CaMn_{0.9}Mg_{0.1}O_2 + a/2CO_2 + aH_2O \tag{7}$$

$$CaMn_{0.9}Mg_{0.1}O_2 + a\,O_2 \rightarrow CaMn_{0.9}Mg_{0.1}O_{2.9} \tag{8}$$

where a 0.9/2. If fuel air mixing is well prevented by the loop seals, the reduction (Eq. (7)) occurs in the fuel reactor, whereas the oxidation (Eq. (8)) only occurs in the air reactor. In both zones, as reactions proceed, the particle mass, and the mass fractions of the oxidized ($CaMn_{0.9}Mg_{0.1}O_{2.9}$) and reduced ($CaMn_{0.9}Mg_{0.1}O_2$) contributions inside the particle also change. Thus, two solid species mass fractions, Y_{ox} for the oxidized species and Y_{red} for the reduced species, are defined and must satisfy the relationship $Y_{ox} + Y_{red}$ 1. Because the amounts of oxidized and reduced species are related to each other via the mass of the oxygen carrier, only one appropriate scalar defined in the particulate phase is sufficient to predict the particle mass and its composition. This scalar is the mean number of particles per unit mass, non dimensionalized by a reference constant mass, namely X_d m_p^{ref}/m_p; m_p is the instantaneous local mean particle mass, and m_p^{ref} $m_{p_{red}}^F$ is the mass of the fully reduced OC, which is equal to a known value. Assuming that the particles do not undergo attrition or break up phenomena, the evolution of the dimensionless mean number of particles per unit solid mass is governed by the following equation:

$$\alpha_p\rho_p\left(\frac{\partial X_d}{\partial t} + U_{p,j}\frac{\partial X_d}{\partial x_j}\right) \quad \frac{\partial}{\partial x_j}\left(\alpha_p\rho_p D_p^{kin}\frac{\partial X_d}{\partial x_j}\right) \quad X_d\Gamma_p \tag{9}$$

in which D_p^{kin} denotes the diffusivity coefficient because of the transport of X_d by particle velocity fluctuations. The solution of the above equation provides an update of the particle properties during simulations at each time step. These properties include the particle mass, the mass fractions of reduced and oxidized species, solid conversions, and particle oxidation degree. The computation of such properties is briefly explained here, whereas that of the mass exchange, Γ_p, is detailed later in Section 3.3. The mean mass fractions of oxidized and reduced species are written in terms of their respective instantaneous masses, ($m_{p_{ox}}$ and $m_{p_{red}}$), and that of the total mass, m_p:

$$Y_{ox} \quad m_{p_{ox}}/m_p, \qquad Y_{red} \quad m_{p_{red}}/m_p. \tag{10}$$

The conversions of oxidized and reduced species during the reduction and oxidation reactions (Eqs. (7) and (8)), respectively, are defined as

$$X_r \quad \left(m_{p_{ox}}^F \quad m_{p_{ox}}\right)/m_{p_{ox}}^F, \qquad X_o \quad \left(m_{p_{red}}^F \quad m_{p_{red}}\right)/m_{p_{red}}^F, \tag{11}$$

where $m_{p_{ox}}^F$ is the mass of fully oxidized OC. By introducing the degree of oxidation

$$X \quad \frac{m_p \quad m_{p_{red}}^F}{m_{p_{ox}}^F \quad m_{p_{red}}^F}, \tag{12}$$

and accounting for mole conservation, $m_{p_{red}}^F/W_{red}$ $m_{p_{ox}}^F/W_{ox}$ $m_{p_{red}}/W_{red} + m_{p_{ox}}/W_{ox}$, the relationships between X and conversion quantities can be obtained as follows:

$$X \quad X_o \quad 1 \quad X_r. \tag{13}$$

Finally, from Eqs. (10) (13), the following expressions may be obtained for mass fractions:

$$Y_{ox} \quad \frac{1 \quad X_d}{1 \quad \left(m_{p_{red}}^F/m_{p_{ox}}^F\right)}, \qquad Y_{red} \quad \frac{X_d \quad \left(m_{p_{red}}^F/m_{p_{ox}}^F\right)}{1 \quad \left(m_{p_{red}}^F/m_{p_{ox}}^F\right)}. \tag{14}$$

The instantaneous mean particle density is then obtained using the relationship ρ_p $6m_{p_{red}}^F/(\pi d_p^3 X_d)$, assuming a constant particle diameter d_p $d_{p_{ox}}$. Although this assumption is retained in the present study, the modeling is developed in such a way that an additional evolution equation for the particle diameter may be considered as well.

3.3. Interphase mass transfer

According to reactions (7) and (8), the mass transfer rate per unit volume, Γ_p $\Gamma_p^{(r)} + \Gamma_p^{(o)}$, is composed of two contributions: the first, ($\Gamma_p^{(r)}$), is because of the reduction, and the second, ($\Gamma_p^{(o)}$), is because of the oxidation. These contributions are related to the consumption rates, Φ_{ox} and Φ_{red} (in kg/m^3/s), of the oxidized and reduced species by the following relationships: $\Gamma_p^{(r)}$ $\Phi_{ox}^{(r)} + \Phi_{red}^{(r)}$, $\Gamma_p^{(o)}$ $\Phi_{ox}^{(o)} + \Phi_{red}^{(o)}$. The mass conservation during the chemical

reactions imposes that Φ_{ox}/W_{ox} Φ_{red}/W_{red}. Combining these expressions makes it possible to write each mass transfer rate contribution as a function of the reactant species consumption rate involved in each reaction:

$$\Gamma_p^{(r)} \quad \left(1 \quad \frac{W_{red}}{W_{ox}}\right)\Phi_{ox}^{(r)}, \quad \Gamma_p^{(o)} \quad \left(1 \quad \frac{W_{ox}}{W_{red}}\right)\Phi_{red}^{(o)}$$
$$\Gamma_p \quad \left(1 \quad \frac{W_{red}}{W_{ox}}\right)\Phi_{ox}^{(r)} + \left(1 \quad \frac{W_{ox}}{W_{red}}\right)\Phi_{red}^{(o)}. \tag{15}$$

The modeling of consumption rates, $\Phi_{ox}^{(r)}$ and $\Phi_{red}^{(o)}$, is detailed in Section (3.7).

3.4. Gas mixture species evolution

The evolution of gaseous species is predicted using N transport equations, written as follows:

$$\alpha_g\rho_g\left(\frac{\partial Y_\alpha}{\partial t} + U_{gj}\frac{\partial Y_\alpha}{\partial x_j}\right) \quad \frac{\partial}{\partial x_j}\left(\alpha_g\rho_g D_\alpha^{eff}\frac{\partial Y_\alpha}{\partial x_j}\right) \quad Y_\alpha\Gamma_g + \Psi_\alpha, \tag{16}$$

where Y_α represents the mass fraction of species, α, in the gas mixture and Ψ_α accounts for the change in species mass fractions because of chemical reactions; D_α^{eff} represents an effective diffusivity composed of a laminar and turbulent contribution, $D_\alpha^{eff} \quad D_\alpha^l + D_\alpha^t$. The turbulent contribution D_α^t is assumed equal to the gas turbulent viscosity (Vermorel et al., 2003) divided by a given turbulent Schmidt number, σ^t, which is taken equal to unity in this work: $D_\alpha^t \quad \nu_g^t$. The density of the gaseous mixture is computed by the perfect gas law, $\rho_g \quad \left(\sum_\alpha^N {}_1 Y_\alpha/W_\alpha\right)^1 P_{ref}/(R_g T_g)$, where W_α is the molar mass of species α. According to reactions (7) and (8) and because air is used as an oxidant in the air reactor, $N \quad 5$ gaseous species are retained: CH_4, CO_2, H_2O, O_2, and N_2. As no gaseous reaction was considered in this study, the source term, Ψ_α, in Eq. (16) is purely an interphase mass transfer of α^{th} species from the reactive particulate phase to the gas phase. Such a source term is defined as $\Psi_\alpha \quad \Psi_\alpha^{(r)} + \Psi_\alpha^{(o)}$ and defined for each species, as follows: $\Psi_{CH_4} \quad \Psi_{CH_4}^{(r)} \quad \frac{a}{2}\frac{W_{CH_4}}{W_{ox}}\Phi_{ox}^{(r)}$, $\Psi_{CO_2} \quad \Psi_{CO_2}^{(r)} \quad \frac{a}{2}\frac{W_{CO_2}}{W_{ox}}\Phi_{ox}^{(r)}$, $\Psi_{H_2O} \quad \Psi_{H_2O}^{(r)} \quad a\frac{W_{H_2O}}{W_{ox}}\Phi_{ox}^{(r)}$, $\Psi_{O_2} \quad \Psi_{O_2}^{(o)} \quad a\frac{W_{O_2}}{W_{red}}\Phi_{red}^{(o)}$ and $\Psi_{N_2} \quad 0$, because $\Psi_{CH_4}^{(o)} \quad 0, \Psi_{CO_2}^{(o)} \quad 0, \Psi_{H_2O}^{(o)} \quad 0, \Psi_{N_2}^{(r)} \quad \Psi_{N_2}^{(o)} \quad 0$.

3.5. Interphase enthalpy transfer because of interphase mass transfer

The enthalpy H_σ represents the mass enthalpy of the mass flux crossing the particle surfaces. Its modeling is detailed in this section. It was assumed that the reactant species, CH_4 and O_2, cross the interface at the gas temperature (T_g), whereas the product species, CO_2 and H_2O, cross the interface at the particulate phase temperature (T_p). This leads to

$$H_\sigma\Gamma_g \quad H_{CH_4}(T_g)\Psi_{CH_4} + H_{CO_2}(T_p)\Psi_{CO_2} + H_{H_2O}(T_p)\Psi_{H_2O} + H_{O_2}(T_g)\Psi_{O_2}. \tag{17}$$

Because $\Gamma_g \quad \Gamma_p$, the mass enthalpy, H_σ, is computed as follows:

$$H_\sigma \quad \frac{a}{2}\frac{\Phi_{ox}^{(r)}}{\Gamma_p}\left[\frac{W_{CO_2}}{W_{ox}}H_{CO_2}(T_p) + 2\frac{W_{H_2O}}{W_{ox}}H_{H_2O}(T_p) \quad \frac{W_{CH_4}}{W_{ox}}H_{CH_4}(T_g)\right] \quad a\frac{W_{O_2}}{W_{red}}\frac{\Phi_{red}^{(o)}}{\Gamma_p}H_{O_2}(T_g). \tag{18}$$

3.6. Local mean phase temperature determination

The mass enthalpy, H_g, of the gaseous mixture composed of N chemical species α, each one associated to a mass enthalpy H_α, may be related to the gas temperature, T_g, by the following expression:

$$H_g \quad \sum_\alpha^N {}_1 Y_\alpha H_\alpha(T_g). \tag{19}$$

According to Shomate equations, the mass enthalpy of each species can be expressed as a function of the gas temperature by the following polynomial:

$$H_\alpha(t_g) \quad H_\alpha(T_{ref}) \quad \frac{1000}{W_\alpha}[At_g + Bt_g^2/2 + Ct_g^3/3 + Dt_g^4/4 \quad E/t_g + F \quad H], \tag{20}$$

in which $t_g \quad T_g/1000$ and A to H are coefficients for each species available from the literature (Web site of the NIST). A comparison among enthalpies as obtained from the solution of Eq. (6) for the gas phase and enthalpy as obtained from Eqs. (19) and (20), makes it possible to find the corresponding gas temperature, T_g, using an iterative numerical method. Once the temperature is obtained, the mass heat capacity, C_{p_α}, of each species is updated through a corresponding Shomate equation (Web site of the NIST). The mass heat capacity of the mixture, C_{p_g}, is then obtained as $C_{p_g} \quad \sum_\alpha^N {}_1 Y_\alpha C_{p_\alpha}(T_g)$. For the particulate phase, the change in composition must also be considered. The mass enthalpy of the particulate phase is defined as follows:

$$H_p \quad Y_{ox} \quad \Delta H_{f_{ox}}^0 + \int_{T_{ref}}^{T_p} C_{p_{ox}}(T)\mathrm{d}T\Big) + Y_{red} \quad \Delta H_{f_{red}}^0 + \int_{T_{ref}}^{T_p} C_{p_{red}}(T)\mathrm{d}T\Big), \tag{21}$$

where $C_{p_{ox}}$ and $\Delta H_{f_{ox}}^0$, and $C_{p_{red}}$ and $\Delta H_{f_{red}}^0$ are mass heat capacities and standard formation enthalpies of oxidized and reduced species, respectively. In addition, it was assumed that the particle mass heat capacity, C_{p_p}, is independent of temperature and mass fraction, i.e., $C_{p_p} \quad C_{p_{ox}} \quad C_{p_{red}}$. Therefore, the particulate phase temperature is obtained as follows:

$$T_p \quad T_{ref} + \frac{H_p \quad \left(Y_{ox}\Delta H_{f_{ox}}^0 + Y_{red}\Delta H_{f_{red}}^0\right)}{C_{p_p}}. \tag{22}$$

To the best of our knowledge, the information regarding the standard enthalpy of reaction for the retained perovskite oxygen carrier ($CaMn_{0.9}Mg_{0.1}O_{3\ \delta}$) is deficient. Therefore, some assumptions are required in order to enable the use of Eq. (22) in numerical simulations. The strategy retained in this study is briefly explained here. The mass enthalpies (in J/kg of the reactant solid species) of reduction and oxidation reactions (Eqs. (7) and (8)) under standard conditions are defined, respectively, as follows:

$$\Delta H_r^0 \quad \frac{W_{red}}{W_{ox}}\Delta H_{f_{red}}^0 + \frac{a}{2}\frac{W_{CO_2}}{W_{ox}}\Delta H_{f_{CO_2}}^0 + a\frac{W_{H_2O}}{W_{ox}}\Delta H_{f_{H_2O}}^0 \quad \frac{a}{2}\frac{W_{CH_4}}{W_{ox}}\Delta H_{f_{CH_4}}^0 \quad \Delta H_{f_{ox}}^0,$$
$$\Delta H_o^0 \quad \frac{W_{ox}}{W_{red}}\Delta H_{f_{ox}}^0 \quad a\frac{W_{O_2}}{W_{red}}\Delta H_{f_{O_2}}^0 \quad \Delta H_{f_{red}}^0. \tag{23}$$

The overall reaction in the CLC process is written as follows: $a/2CH_4 + a\ O_2 \rightarrow a/2CO_2 + a\ H_2O$. The heat released by the complete combustion of methane with oxygen under standard conditions (in J/kg of methane) is therefore

$$\Delta H_c^0 \quad \frac{W_{CO_2}}{W_{CH_4}}\Delta H_{f_{CO_2}}^0 + 2\frac{W_{H_2O}}{W_{CH_4}}\Delta H_{f_{H_2O}}^0 \quad 2\frac{W_{O_2}}{W_{CH_4}}\Delta H_{f_{O_2}}^0 \quad \Delta H_{f_{CH_4}}^0. \tag{24}$$

From the above equations, the following can be obtained:

$$W_{red}\Delta H_o^0 + W_{ox}\Delta H_r^0 \quad \frac{a}{2}W_{CH_4}\Delta H_c^0. \tag{25}$$

On the premise that the formation enthalpy of the oxidized species is zero, and the reduction reaction is not accompanied by heat release (this assumption is considerably realistic as the perovskite reduction is known to be a slightly endothermic reaction), the formation enthalpies of solid species are finally computed as follows:

$$\Delta H_{f_{ox}}^0 \quad 0, \qquad \Delta H_{f_{red}}^0 \quad \frac{a}{2}\frac{W_{CH_4}}{W_{red}}\Delta H_c^0 \quad a\frac{W_{O_2}}{W_{red}}\Delta H_{f_{O_2}}^0. \tag{26}$$

In Table 6, the values of standard formation enthalpies and standard enthalpies of reaction used in numerical simulations are summarized.

3.7. Heterogeneous gas solid reaction

In this section, the modeling of solid species consumption rates ($\Phi_{ox}^{(r)}$ and $\Phi_{red}^{(o)}$) is detailed. These quantities are required to close the interphase mass and enthalpy source terms. Their expressions are derived on the basis of the shrinking core model (SCM) in the grains, also called grain model. This model assumes that the particle is composed of a random grouping of non porous grains that react according to SCM. The reaction occurs at a sharp interface between the reacted and unreacted solids, while the interface moves inward leaving behind a solid product layer. de Diego et al. (2014) conducted thermal gravimetric analysis (TGA) experiments in order to determine C14 reactivity and used the grain model to define the kinetics of both reduction and oxidation reactions occurring in the CLC process. In their study, they showed that for this selected oxygen carrier, the overall process of the gas solid reaction is limited by the chemical reaction and diffusion through the product layer surrounding the grains. Therefore, in the present study, both reduction and oxidation reactions were assumed to evolve according to the mechanisms of the chemical reaction onto the grain surface and diffusion of species in the product layer surrounding the unreacted core. Additionally, the external mass transfer of the gaseous species from the gas to the solid particle, through an external film surrounding the particle, was accounted for in the modeling. Finally, the consumption rates of oxidized and reduced species are written as follows (for further details, refer to Hamidouche (2017)):

$$\begin{aligned}\Phi_{ox}^{(r)} &\quad n_p m_{p_{ox}}^F \left\{\tau_{ch,CH_4} + 2\tau_{pl,CH_4}\left[(1 \quad X_r)^{1/3} \quad 1\right] + \tau_{ext,CH_4}(d_{p_{ox}}/d_p)^2\right\}^{1},\\ \Phi_{red}^{(o)} &\quad n_p m_{p_{red}}^F \left\{\tau_{ch,O_2} + 2\tau_{pl,O_2}\left[(1 \quad X_o)^{1/3} \quad 1\right] + \tau_{ext,O_2}(d_{p_{red}}/d_p)^2\right\}^{1},\end{aligned} \tag{27}$$

Table 6
Mass enthalpies of formation and enthalpies of reaction at standard conditions of 1 atm and 298.15 K.

	Species or reactions	ΔH_f^0 or ΔH^0 (kJ/kg)
Gaseous species	CH_4	−4675
	CO_2	−8943
	H_2O	−13,435
	O_2	0
	N_2	0
Solid species	*ox* ($CaMn_{0.9}Mg_{0.1}O_{2.9}$)	0
	red ($CaMn_{0.9}Mg_{0.1}O_2$)	1456.443
Reactions	ΔH_r^0	0
	ΔH_o^0	−1456.443
	ΔH_c^0	−50,143.388

using the empirical chemical and diffusion times (de Diego et al., 2014)

$$\begin{aligned}\tau_{ch,\alpha} &\quad \frac{1}{k_v\left(C_{\alpha,g}^n \quad C_{\alpha,eq}^n\right)} \quad \text{with} \quad k_v \quad k_v^0 \exp\left(\frac{E_{ch}}{R_g T_p}\right)\\ \tau_{pl,\alpha} &\quad \frac{1}{6D_{pl,v}\left(C_{\alpha,g}^{n'} \quad C_{\alpha,eq}^{n'}\right)} \quad \text{with} \quad D_{pl,v} \quad D_{pl,v}^0 \exp\left(\frac{E_{pl}}{R_g T_p}\right),\end{aligned} \tag{28}$$

where the equilibrium concentrations, $C_{\alpha,eq}$, are set equal to zero for both methane and oxygen, as suggested by de Diego et al. (2014). The external transfer times were defined by using the mass transfer coefficient, $k_{m,\alpha}$ (Bird et al., 2007), computed as $k_{m,\alpha} \quad D_\alpha Sh_\alpha/d_p$, where Sh_α is the Sherwood number based on Schmidt and particle Reynolds numbers (Frössling, 1938), and D_α is the laminar mass diffusivity of the species, α, into the major species:

$$\tau_{ext,CH_4} \quad \frac{a/2 d_{p_{ox}}\rho_{p_{ox}}}{6W_{ox}k_{m,CH_4}C_{CH_4}}, \qquad \tau_{ext,O_2} \quad \frac{a d_{p_{red}}\rho_{p_{red}}}{6W_{red}k_{m,O_2}C_{O_2}}. \tag{29}$$

Table 7 summarizes the kinetic parameters of C14 oxygen carrier as obtained from TGA experiments (de Diego et al., 2014), for activated particles retained in this study. The redox mechanisms and relative reaction models implemented in NEPTUNE_CFD code were first validated against experimental TGA results in a zero dimensional (0D) configuration (Hamidouche, 2017) before being used in 3D numerical simulations.

4. Numerical simulations

Unsteady three dimensional numerical simulations of the CLC pilot were performed using the N Euler modeling approach for fluid particle turbulent polydispersed reactive flows implemented in NEPTUNE_CFD V1.08@Tlse version by IMFT (Institut de Mécanique des Fluides de Toulouse). NEPTUNE_CFD is a computational multiphase flow software developed in the framework of the NEPTUNE project, financially supported by CEA (Commissariat à l'Énergie Atomique), EDF (Electricité de France), IRSN (Institut de Radioprotection et de Sûreté Nucléaire) and AREVA NP. The code uses a cell center type finite volume method, with a second order centered scheme in space and a first order scheme in time. The algorithm is based on an elliptic semi implicit fractional step method, using iterative linear solvers or direct matrix inversion. Thereafter, a dynamic time step, based on Courant and Fourier criteria for both gas and dispersed phase, is computed. Although the code employs low order numerical schemes, the use of regular meshes allows the improvement of the accuracy of numerical results. Through several validation campaigns, such an accuracy has been investigated at length over test cases for which analytical or experimental results are available for comparison. Details of the code and its performance may be found elsewhere (Neau et al., 2013; Hamidouche et al., 2018).

Table 7
Kinetic parameters for reactions of $CaMn_{0.9}Mg_{0.1}O_{2.9}$ with CH_4 and O_2 (de Diego et al., 2014).

Parameter	Units	CH_4	O_2
n	-	0.5	1
k_v^0	m^{3n} mol ^{n} s ^{1}	24	0.28
E_{ch}	kJ mol ^{1}	66.1	25.1
n'	-	0	1
$D_{pl,v}^0$	$m^{3n'}$ mol $^{n'}$ s ^{1}	3.2×10^5	4.2×10^{2}
E_{pl}	kJ mol ^{1}	187.8	13.4

The experimental geometry is shown in Fig. 2a. The configura tion retained for numerical simulations is depicted in Fig. 2b. The numerical configuration does not include internal or upper loop seals (ILS and ULS) and cyclones. Their effects are reproduced in simulations by appropriate boundary conditions, resulting in a reduction of computational costs. As for the gas injection, the 3D model used for the simulation represents the same geometry of the gas injection system as the experimental system. The only dif ference is that in the experimental unit, the pipes of the nozzles do not end at the reactor wall (as in the numerical simulation), but are directed some centimeters inside the reactor. In a previous study (Hamidouche, 2017), an analysis was performed on the influence of the steam injection in LLS on global pressure predictions. Results showed that the pressure drop in the whole system was slightly affected by different types of injections (bottom *versus* lateral inlets). In particular, the lateral injection exhibited lower pressure drop values than did the bottom injection. This is the reason for the retention of the same geometry as the experimental system, with the exception of penetrating pipes.

The entire domain is meshed by a grid accounting for approxi mately 1.7 million hexahedra (their approximate sizes are summa rized in Table 8. Such a grid is considered a suitable compromise between a highly refined (highly expensive) mesh, ensuring fully converged results, and a coarse mesh, requiring sub grid scale (SGS) models. In the literature, several SGS models have been pro posed and tested, either under bubbling or fast fluidizing regimes (Igci et al., 2008; Igci et al., 2012; Parmentier et al., 2012; Özel et al., 2013; Schneiderbauer, 2017, for example). In fact, the intri cate behavior inside the CLC system makes the choice of an appro priate one difficult. The CLC system simulated in the present work is indeed based on dual circulation fluidized beds, each one working under a different regime. The fuel reactor operates under a bubbling regime, whereas the air reactor is a typical circulating fluidized bed with a dense region at the bottom of the riser. When a circulating fluidized bed is simulated using a coarse grid, the solid mass flow rate is generally overestimated because of the over prediction of the drag force, which is because of the lack of resolution in small scale structures in the dispersed phase (because of the SGS correlation between the solid volume fraction and gas velocity). In the present study, the mass flow rate is a result of the numerical simulation, because only the solid mass is imposed at the initial time. Consequently, a larger value should be expected if small scale structures were not well resolved. Numerical predic tions (presented in Section 5) will show instead that the mean solid mass flow rate at the AR outlet compares well with experimental measurements, demonstrating the suitability of the selected grid. A coarse mesh used in a bubbling regime would lead instead to an overestimation of the fluidized bed height. In the present numerical simulation, it cannot be excluded that a higher bed height is predicted in FR; however, this problem cannot be resolved by comparing it with experimental data because more pressure drop measurements would be necessary to estimate the actual bed height. Additionally, the behavior of the particulate flow

Table 8
Details of the mesh size.

	FR	AR	LLS	Connections
Δ_x (cm)	0.52	0.52	0.25	[0.28–0.52]
Δ_y (cm)	0.62	0.62	0.52	[0.32–0.62]
Δ_z (cm)	0.50	0.50	0.25	[0.25–0.50]
N° of cells	645,720	886,800	56,320	134,400

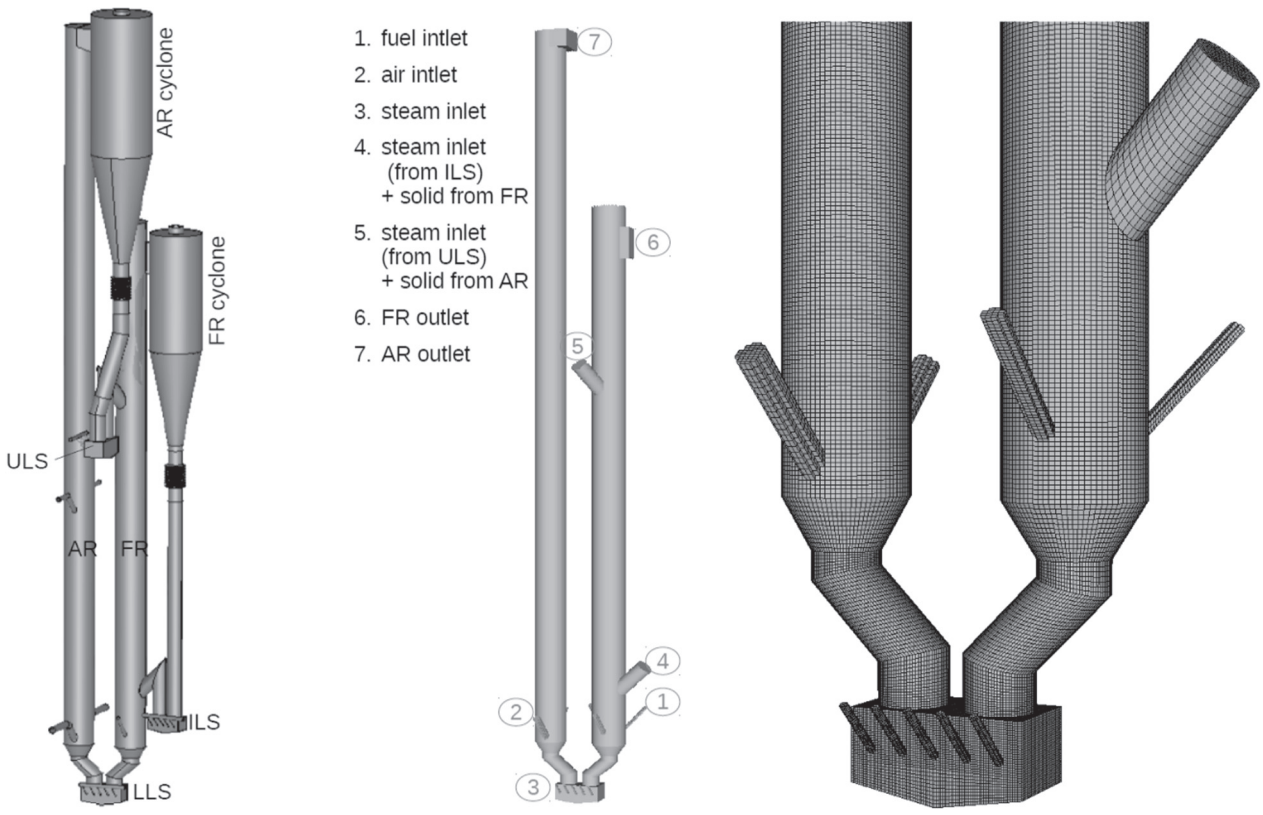

(a) Experimental geometry (b) Numerical configuration (c) Zoom on the lower part mesh

Fig. 2. Numerical *versus* experimental configurations.

in such a dense zone is sensibly modified by lateral injections, which make bubbles form and move inside the bed before splash ing onto the bed surface. This mechanism promotes mixing, and should therefore limit the effects of a coarse grid. A magnified view of the lower part of the system and its meshing is shown in Fig. 2c.

Both gas and particulate phases were initialized at a tempera ture of 1223 K. The entire system was filled with nitrogen. Because both ULS and ILS were not considered in the numerical configura tion, the system was loaded with an amount of (partially oxidized) solid, which was less than the total amount reported in the exper iments (Table 3). For the fuel and air reactors, the experiments sug gested active inventories of 13.5 and 6.5 kg, respectively; however, no experimental data were available for LLS. The experiments fur ther indicated (Table 2) that the bulk density of the oxygen carrier material was equal to 1542 kg/m^3. This made it possible to esti mate a solid mass of approximately 9 kg in the LLS box and 13 kg in the LLS device (LLS box + connection pipes with reactors) under quiescent conditions. Under operating conditions with fluidizing steam, these amounts should be lower than those under quiescent conditions. Therefore, two values of the solid inventory (5 and 10 kg) in the LLS device were tested in the numerical simulations and were found to correspond to total solid masses of 25 and 30 kg, respectively, in the entire CLC system. Such preliminary numerical tests demonstrated that an initial mass of 25 kg led to an underestimation of the solid inventory in both fuel and air reac tors (not shown), whereas a total mass of 30 kg at initialization resulted to satisfactory predictions in both reactors (shown in Sec tion 5). This was the reason for the final retention of a total solid mass of 30 kg.

Mass fractions at the fuel gas inlet were imposed according to experiments (Table 4), considering the heavier hydrocarbons, C_xH_y, as methane. At the air inlet, 23.2 wt% of oxygen and 76.8 wt% of nitrogen were injected. At the CLC bottom, fluidizing steam was injected into LLS according to experimental values (Table 5). The fluidizing steam corresponding to ULS and ILS was directly injected into the reactors. For all these, inlet pure steam corresponding to a mass fraction equal to unity was used. Table 9 summarizes the mass fractions of gaseous species at various inlets of the CLC sys tem. At each time step of the simulation, the mass flow rate (kg/ s) of solid leaving AR was computed by integrating the local and instantaneous solid mass flux (kg/(m^2 s)) over the surface of the reactor outlet (referred to as ⑦ in Fig. 2b). Thereafter, the solid leaving AR was injected into FR by imposing such a solid mass flow rate at the inlet of the pipe (⑤ in Fig. 2b), which connects FR with ULS (not simulated in the present work). Similarly, the mass flow rate of solids leaving FR was computed at each time step, and the solid was re injected into FR by imposing such an inlet condi tion at the pipe connecting FR with ILS (④ in Fig. 2b). Through these inlets (connection pipes), the fluidizing steam was injected into FR, together with the solid. The amount and temperature of steam at each inlet (⑤ and ④) correspond to those obtained from the experiments, as summarized in Table 5 (ULS and ILS, respec tively). For both inlets, a temperature of 950 °C was instead set for the solid. This temperature corresponded to that of the selected operating point. During the simulation, a fixed pressure difference was imposed between the two reactor outlets (⑦ and ⑥), and its value (ΔP 265.5 Pa) corresponded to the difference among the experimental pressure drops at these locations. The inlets (⑤ and ④) did not require any pressure specification; pressure gradi ent extrapolations were made directly by the code.

Table 9
Inlet mass fractions at the CLC system.

Mass fractions	Fuel inlet	Air inlet	Steam inlets
Y_{CH_4}	0.975	0	0
Y_{CO_2}	0.007	0	0
Y_{H_2O}	0	0	1
Y_{O_2}	0	0.232	0
Y_{N_2}	0.0018	0.768	0

In the experimental unit, the presence of reactor cyclones and their corresponding downcomers may affect steam flows, as well as pressure drops. In fact, a part of the steam injected by the noz zles in ILS may move upward in the FR downcomer and leave the system through the FR cyclone. The same may occur in ULS. As a consequence, the amount of steam entering FR should be less than that injected into the upper and internal loop seals (specifically, less than that imposed in the numerical simulation). This should affect the pressure distribution in the reactors and consequently change the steam splitting from LLS toward the reactors, as well as the global and internal solid circulations. However, as the cor rect pressure difference between the two reactors was imposed in the numerical simulation, deviations from the experiments because of the amount of the steam injected in FR should be lim ited, as confirmed by numerical results presented in Section 5.

The enthalpy boundary conditions for the particles and gas in AR approximately represented the external cooling effect by forced convection according to a given wall temperature fixed uniformly at 950 °C and separate gas and particle wall heat exchange coefficients expressed in terms of phase variables at the first interior computational cell, $h_{p\to w}$ $\alpha_p\rho_pC_{p_p}K_p^{eff}/|y$ $y_w|$, $h_{g\to w}$ $\alpha_g\rho_gC_{p_g}K_g^{eff}/$ $|y$ $y_w|$, where $|y$ $y_w|$ represents the distance between the wall and first interior computational cell.

As for the fuel reactor, according to previous assumptions, no heat release during the reduction reaction and no heat flux at the wall were considered. Finally, for the solid phase, no slip wall boundary conditions for the mean particle velocity and no zero flux boundary conditions for the particle kinetic energy were retained, as they were found to be considerably effective to account for the wall roughness effect under the particle wall boundary conditions (Fede et al., 2016).

5. Results and discussions

In this section, the results obtained from three dimensional unsteady numerical simulations are presented and discussed. The simulations were aimed at analyzing the thermo hydrodynamic and reactive features of the CLC system in order to gain insight into the CLC process. Averaged quantities and mean profiles were com puted and compared with available experimental measurements. Experimental data reported in the figures represented a steady state operating point obtained by considering an average over the entire interval. Local and instantaneous fields were also ana lyzed in order to study the local behavior of the CLC system, espe cially in those zones that represent critical locations for the CLC design.

In the experiments, the amount of solid inventory in each reac tor was obtained from pressure drop measurements in fluidized beds. Such results are summarized in Table 3. In the numerical simulations, the total mass was calculated from these values and from an estimate of the mass contained in LLS (as previously described). Time evolutions of the solid mass in the air and fuel reactors are shown in Fig. 3a. The results showed that the simula tion, which used 30 kg as a solid inventory, matched well with experimental measurements. Time evolutions of the solid mass in LLS with and without connection pipes were also computed. Results are depicted in Fig. 3b. As previously mentioned, under quiescent conditions, the solid amounts in the LLS device and box were estimated as 13 and 9 kg, respectively. Under operating conditions in which the steam injection in LLS was 2 kg/h at a temperature of 453 K, lower amounts were instead observed

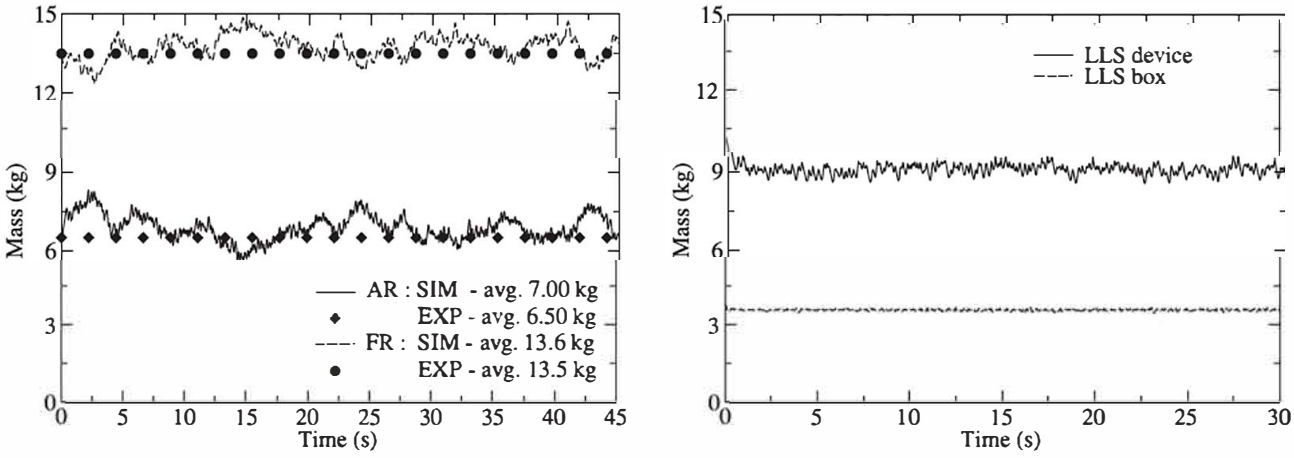

Fig. 3. Time evolutions of the solid mass in the CLC system.

(approximately 9 and 3.6 kg, respectively). It was noteworthy that these amounts had the same values irrespective of the total solid mass inventory; whether 25 or 30 kg (not shown). Time evolutions of the difference between the instantaneous mass ($M(t)$) and its time average (M_{avg}), computed within three different sections of the CLC pilot, are given in Fig. 4. An oscillating behavior of the solid mass was observed. In particular, the results showed low frequency mass fluctuations in both air and fuel reactors, which were approximately 180° out of phase with each other, whereas a high frequency behavior was observed in LLS. Simulations using 25 and 30 kg of the total inventory mainly differed from each other in both reactors in mass fluctuation amplitudes, which depended on the relative solid mass flow rate (not shown). The oscillation amplitudes in LLS were instead found lower and independent of the solid mass flow rate compared with those in the two reactors. However, it should be noted that the numerical simulations did not account for cyclones, which could function as a low pass filter of mass fluctuations, depending on the characteristic residence times. This is an aspect that deserves further investigation.

Fig. 5 shows the mean pressure drop profiles in both reactors along the axial direction, as predicted by the numerical simulation. The experimental measurements are also displayed for the purpose of comparison. A difference with respect to the experimental data was observed at the bottom of the fuel reactor (for z 0). This dif ference might be attributed to the fact that in the experiments, the steam was injected by means of penetrating pipes through LLS, which was not the case in the numerical simulations. Nevertheless, results were globally satisfactory and reproduced both dense and circulating behaviors in FR and AR, respectively.

The time evolutions of solid mass flow rates at the reactor out lets are plotted in Fig. 6a and b. The mass flow of solid leaving AR considerably fluctuated around a mean value, which approximated the value measured in the experiments; however, it was practically zero at the FR outlet. In the experiments, the solid flux was not accessible in FR. The global solid mass flow was derived from the mass and energy balances, especially the oxygen balance, with the aid of OC samples taken from ULS and LLS, and allowed the determination of the oxidation state of OC leaving AR and FR. A detailed description of the solid sampling, and determination of the solid circulation rate and the evaluation process are given else where (Kolbitsch et al., 2009b; Penthor et al., 2015). Results from the numerical simulation confirm the operating regime of the two reactors, that is, AR behaves as a circulating fluidized bed and FR as a bubbling fluidized bed, as expected. This can also be qualitatively observed in Fig. 7, which represents a snapshot of the local instantaneous solid volume fraction at the end of the numerical simulation. Numerical results also confirm the appropri ateness of the selected mesh and injection conditions. In fact, numerical predictions showed that the mean solid mass flow rate

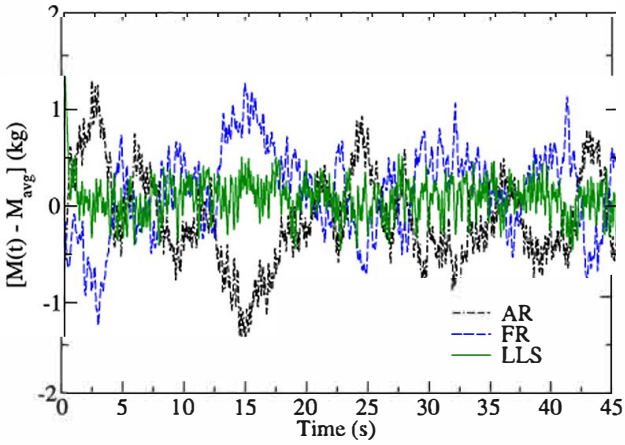

Fig. 4. Time evolutions of mass fluctuations in the CLC system.

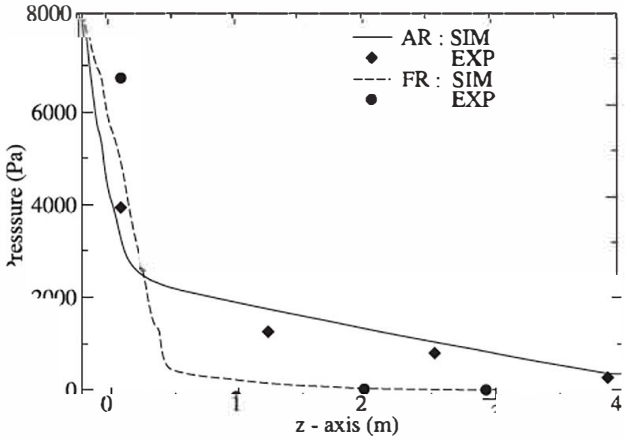

Fig. 5. Mean gas pressure-drop axial profiles.

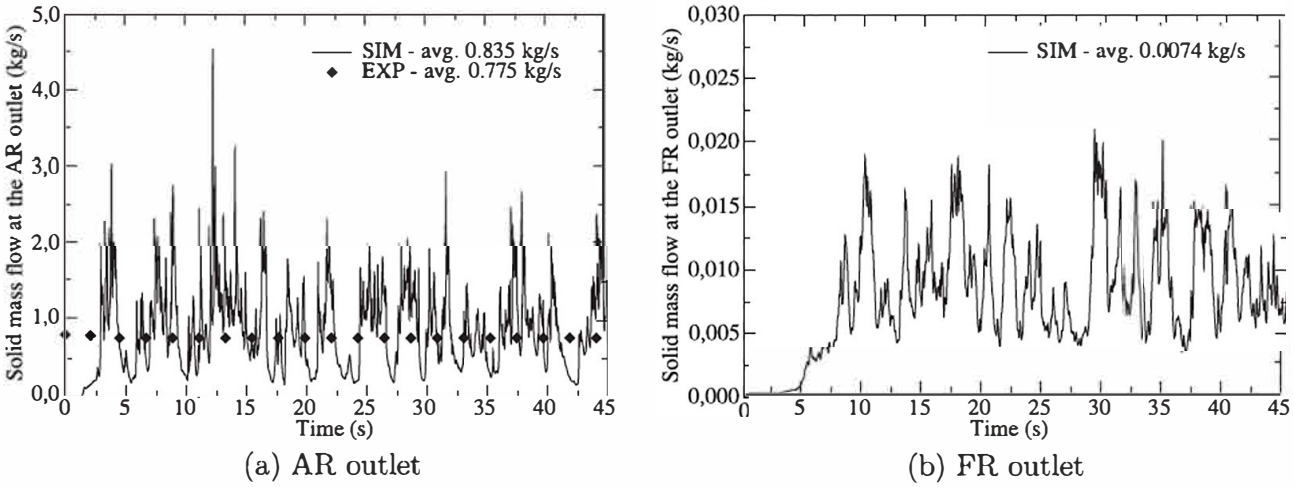

Fig. 6. Time evolution of solid mass flow rates leaving the reactors.

at the AR outlet compared considerably well with experimental measurements (Fig. 6a). The slight overestimation of the mean mass flow rate (numerical (0.835 kg/s) against experimental (0.775 kg/s)) was actually consistent with the slight overestimation of the solid mass in AR (numerical (7 kg) against experimental (6.5 kg)), and therefore, should not be attributed to unresolved scales or injection amounts. The time averaged mass flux at the AR outlet predicted by the simulation was 48.29 kg/m^2/s. This result, compared with the experimental value of 43.85 kg/m^2/s, showed that the simulation agreed reasonably well with experimental measurements in terms of global solid circulation.

Concerning thermodynamics and reactions, the most relevant parameters of the CLC process were the degree of oxidation, methane conversion, CO_2 yield, and gas temperature in the reactors. Numerical results of such quantities obtained from the numerical simulation were analyzed and compared with experimental measurements. The time evolutions of the oxidation degree at the top of AR (or in ULS) and in LLS are shown in Fig. 8. Results showed that numerical predictions matched considerably well the experimental measurements at the top of AR and closely approximated the experimental measurements in LLS at the end of the simulation. A local view of the oxidation degree is given in Fig. 9. The oxygen carrier entered FR with an oxidation degree of approximately 90% and reacted with methane throughout its reduction and during its stay in the dense zone of FR; the pressure drop between the beds and LLS operation mode promoted the flow of the reduced material from FR into AR for regeneration.

The methane conversion (χ_{CH_4}) and carbon monoxide yield factor (Υ_{CO_2}) at the fuel reactor outlet are defined by the following relations:

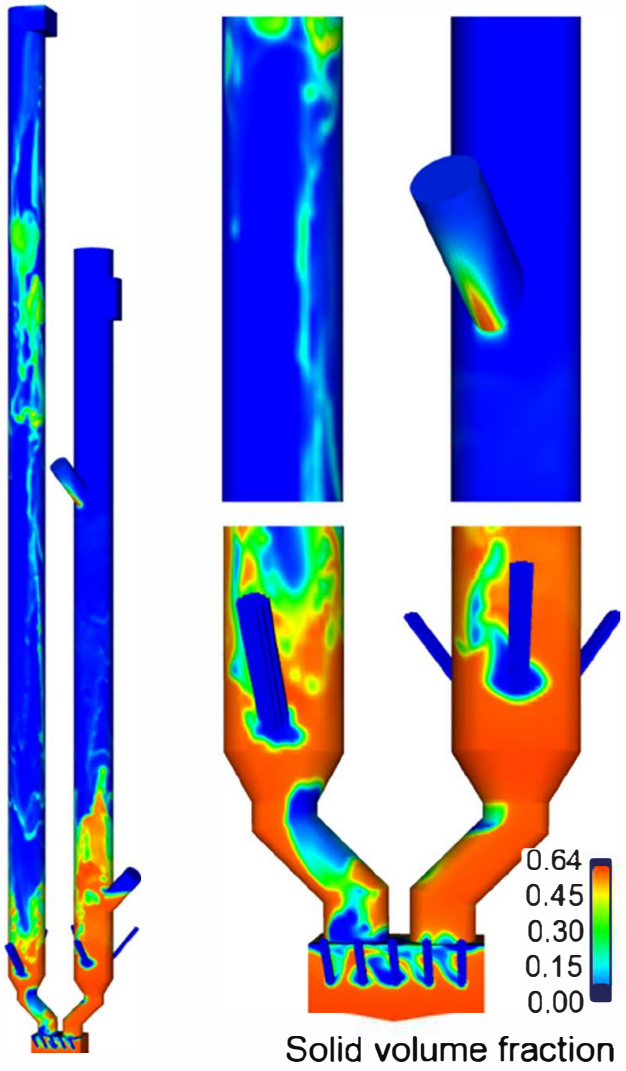

Fig. 7. Local and instantaneous solid volume fraction in the CLC system at the end of the numerical simulation.

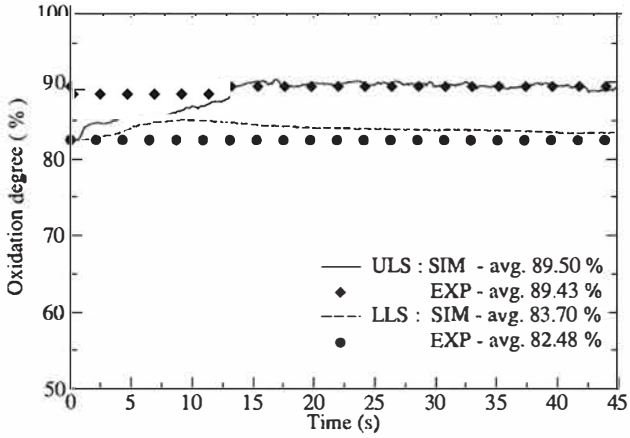

Fig. 8. Time evolution of the oxidation degree at the top of AR and in LLS.

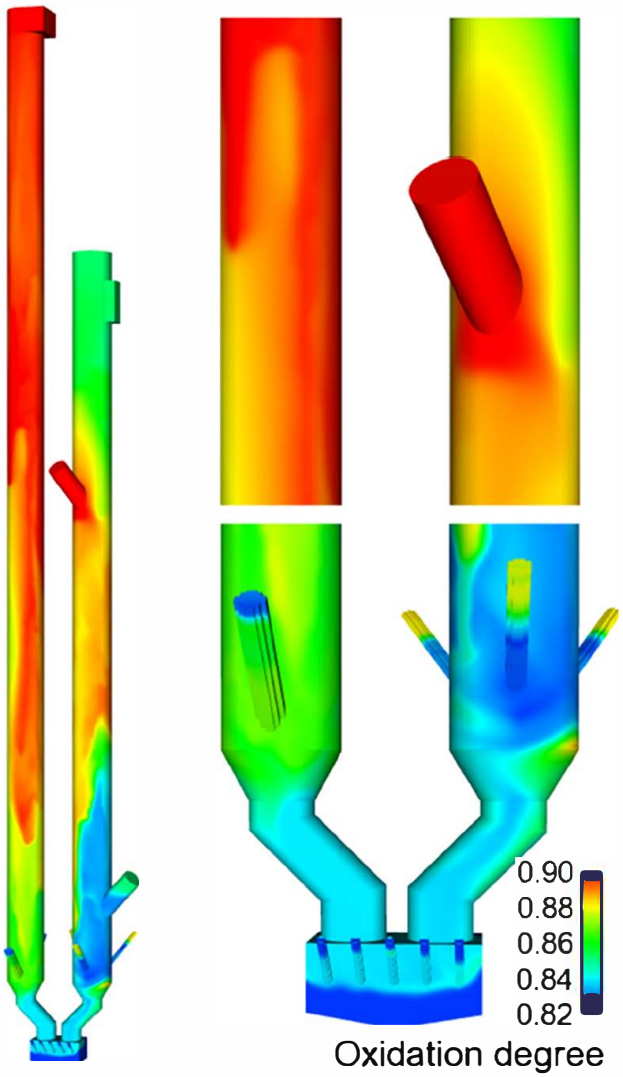

Fig. 9. Local and instantaneous oxidation degree in the CLC system at the end of the numerical simulation.

$$\chi_{CH_4} \quad 1 \quad X_{CH_4,out}/(X_{CH_4,out} + X_{CO_2,out} + X_{CO,out})$$
$$\Upsilon_{CO_2} \quad X_{CO_2,out}/(X_{CH_4,out} + X_{CO_2,out} + X_{CO,out}), \qquad (30)$$

where $X_{\alpha,out}$ is the mean molar fraction of the species, α, at the fuel reactor outlet. However, because the kinetic mechanism retained in this study to describe the oxygen carrier reduction did not consider the carbon monoxide formation (see Section 3.2) and $X_{CO,in}$ 0 at the fuel reactor inlet, then, $\chi_{CH_4} \equiv \Upsilon_{CO_2}$. Therefore, for the purpose of comparison, only the methane conversion was retained. The time evolution of the methane conversion at the fuel reactor outlet, including the corresponding time averaged value is depicted in Fig. 10. Results showed that the fuel conversion was overestimated by the numerical simulation when compared with experiments. The reason for such a difference are investigated below. The oxygen mass transfer rates, $\varphi_{O_2}^{(r)}$ and $\varphi_{O_2}^{(o)}$, corresponding to the mass loss of OC during the reduction and that gained by OC during the oxidation (per hour), respectively, were computed from the numerical simulation and integrated over the domain corresponding to FR of the former and to AR of the latter. The results, including temporal averages, are depicted in Fig. 11a and b. They showed that in FR, the numerical simulation predicted a slightly higher amount of the oxygen mass transferred from the solid to the gas phase, when compared with experimental measurements (Fig. 11a). It was presumed that such a difference was sufficiently high to justify the overestimation of the fuel conversion at the FR outlet. Moreover, results showed that the oxygen mass transfer rate in FR was higher than that in AR, which meant that the overall reaction consumed oxygen. Consequently, an increase in the reduced species was anticipated during the simulation in the system, and the mass of the oxygen carrier was expected to progressively slow down at a rate corresponding to the overall oxygen mass transfer rate in the whole CLC system. However, this meant that a statistically stationarity state was not reached by each solid contribution, as can be observed in Fig. 12a and b, which show the time evolutions of the relative mass of reduced and oxidized species during the numerical simulation.

To ensure that numerics was not the reason for such a mass variation, mass conservation was investigated. A budget analysis was conducted in AR, FR, and LLS (not shown). The results showed that the solid mass was well conserved and that any mass change was only because of the interphase mass transfer between solid and gas (Γ_p). The slow mass variation, imperceptible on the total mass and visible only on each contribution by a relatively small percentage, was therefore attributed to the low physical time reproduced by the numerical simulation.

In order to further investigate the question of stationarity, the total amounts of atomic oxygen contained in the gas ($M_{O,g}$) and solid ($M_{O,s}$) in each part of the CLC system were computed. Their time evolutions are depicted in Fig. 13a and b, respectively. The foregoing quantities were obtained using the following expressions:

$$M_{O,g} \quad \iiint_V \left(Y_{O_2} + \frac{1}{2}\frac{W_{O_2}}{W_{H_2O}} Y_{H_2O} + \frac{W_{O_2}}{W_{CO_2}} Y_{CO_2}\right) \alpha_g \rho_g dV \qquad (31)$$

$$M_{O,s} \quad \iiint_V \left(\frac{2.9}{2}\frac{W_{O_2}}{W_{ox}} Y_{ox} + \frac{W_{O_2}}{W_{red}} Y_{red}\right) \alpha_p \rho_p dV, \qquad (32)$$

where V can represent the fuel reactor volume, air reactor volume, LLS volume, or overall volume of the CLC system. After a few seconds of numerical simulation, the atomic oxygen amount in both phases seemed to have considerably evolved steadily in each part of the system, similar to that observed in the solid mass (Fig. 3). However, the results, such as those shown in Fig. 11a and b, made it possible to estimate the mean global oxygen transfer rate of 3.1 kg/h from the solid to the gas phase in the whole CLC. The atomic oxygen in the solid, as well as the total solid mass, decreased gradually with time. This quantity corresponded to 0.038 kg of oxygen lost during the numerical simulation (45 s), which represented only 0.127% of the total solid inventory. Such a reduction was therefore

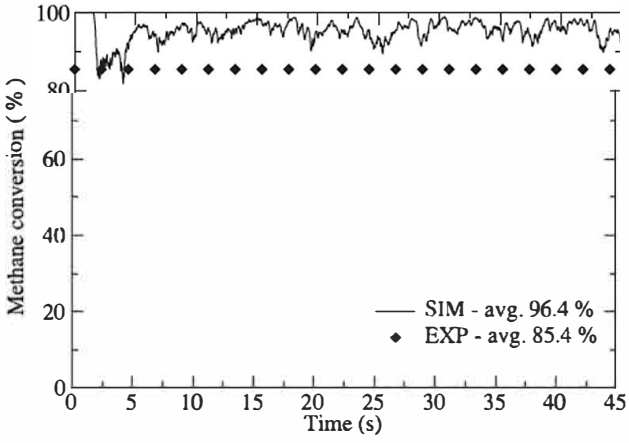

Fig. 10. Numerical against experimental results of the methane conversion at the fuel reactor exit.

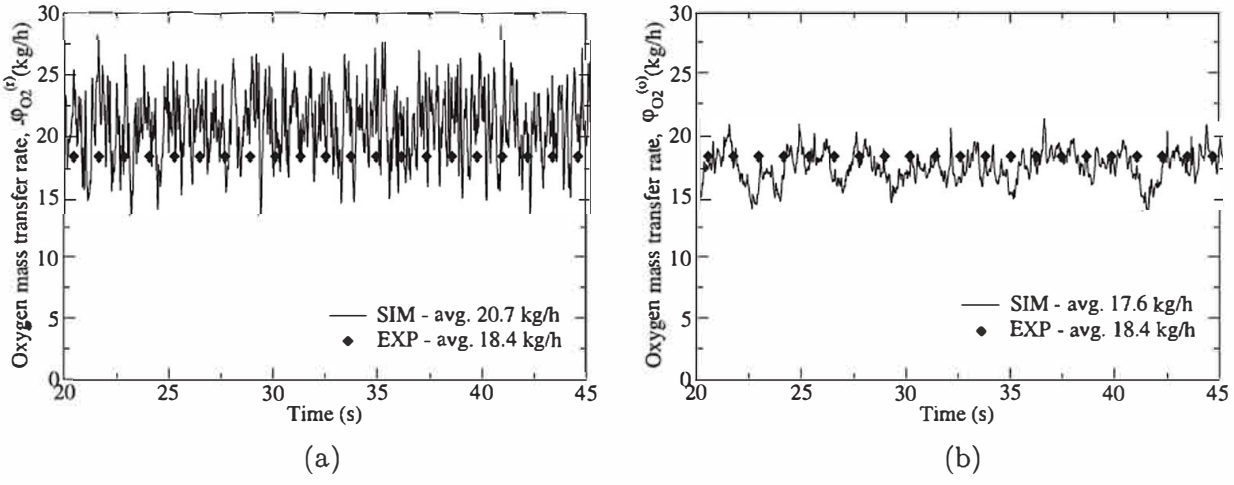

Fig. 11. Numerical against experimental oxygen transfer rates during (a) reduction in the fuel reactor and (b) oxidation in the air reactor.

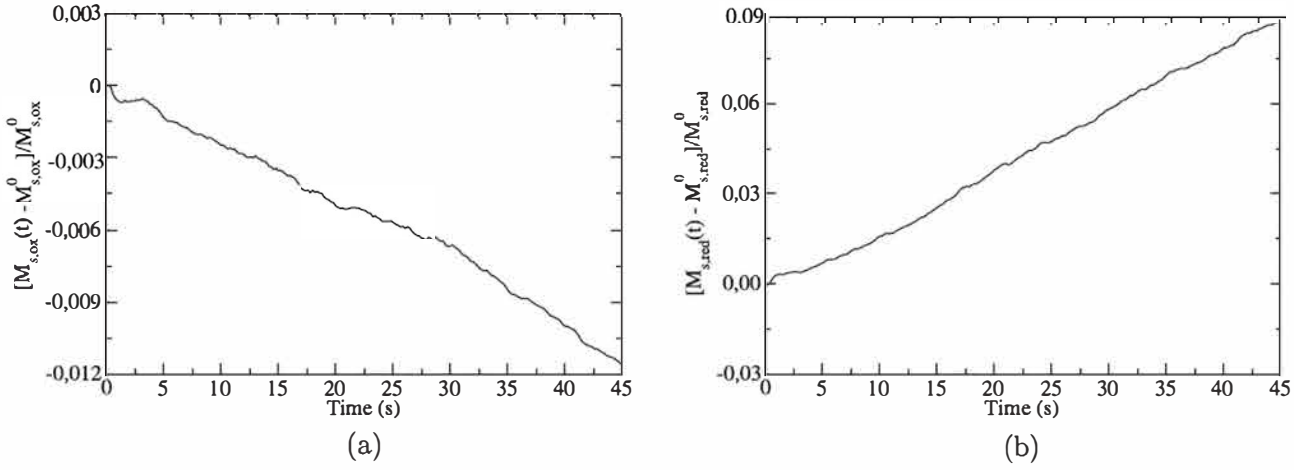

Fig. 12. Time evolutions of the relative mass of (a) oxidized and (b) reduced species in the whole CLC.

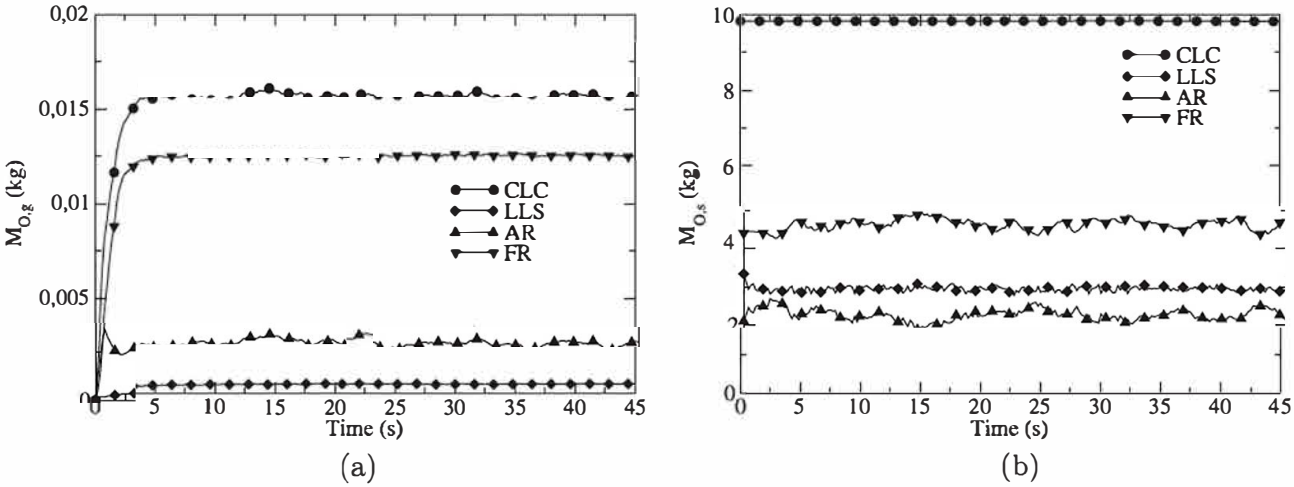

Fig. 13. Time evolutions of the atomic oxygen in gas and solid phases.

imperceptible in the related figures. The numerical simulation identified a long transient behavior, which was intimately related to characteristic time scales inherent to the process. Among these, the most important were the solid residence time, and reduction and oxidation times, which may be estimated as follows: $\tau_{solid} \quad M_s/q_s$; $\tau^{(r)} \quad M_{s,ox}/\varphi_{ox}^{(r)}$; $\tau^{(o)} \quad M_{s,red}/\varphi_{red}^{(o)}$ with $\varphi_{ox}^{(r)} \quad a\varphi_{O_2}^{(r)}W_{ox}/W_{O_2}$ and $\varphi_{red}^{(o)} \quad a\varphi_{O_2}^{(o)}W_{red}/W_{O_2}$; (a = 0.9/2), where M_s and q_s are

Table 10
Reaction and solid residence characteristic times (in s). Values in brackets refer to times reported by the experiments.

Air reactor		Fuel reactor	
Residence time	Reaction time	Residence time	Reaction time
8.20 (8.43)	18.5	15.9 (17.38)	218.40

the total solid inventory and global solid circulation, respectively. Their values in each reactor are listed in Table 10.

The results showed that in the CLC system, the reaction time was considerably higher than the residence time, especially in FR. Moreover, the reduction time (FR) was found to be larger than the simulation time, which meant that a longer simulation time was required in order to ensure a statistically stationary state. The CPU time corresponding to numerical simulations of the pre sent study (25 and 30 kg) amounted to approximately one million hours with the use of 200 cores. Previous studies (Hamidouche et al., 2018) showed that NEPTUNE_CFD HPC performances were excellent while the cell number per core was higher than 8200 (200 cores corresponded to 8500 cells per core). Thus, a fully statis tically stationary regime required considerably high computational costs and a significant amount of wall clock time. The extension of the run is left as a future work.

In summary, the numerical simulation provided considerably satisfactory predictions of the solid mass distribution and global solid circulation mass flow, along with accurate values of the oxi dation degree; however, it overestimated the oxygen mass transfer during the reduction in the fuel reactor. Conceming such an over estimate, an interpretation could be made on the basis of the per ovskite oxygen transference ($\gamma \quad \delta$), accounted for in the modeling. The general form of the reduction reaction (7) can be written as follows:

$$CaMn_{0.9}Mg_{0.1}O_{3\ \delta} + \frac{\gamma \quad \delta}{4}CH_4 \rightarrow CaMn_{0.9}Mg_{0.1}O_{3\ \gamma} + \frac{\gamma \quad \delta}{4}CO_2 + \frac{\gamma \quad \delta}{2}H_2O. \qquad (33)$$

In the numerical simulation, $\delta \quad 0.1$ and $\gamma \quad 1$ were selected, corresponding to the fully oxidized ($CaMn_{0.9}Mg_{0.1}O_{2.9}$) and fully reduced ($CaMn_{0.9}Mg_{0.1}O_2$) forms of the perovskite (de Diego et al., 2014). This meant that a total oxygen transport capacity (R_{oc} with $R_{oc} \quad 1 \quad W_{RED}/W_{OX}$) of 10.4% was considered. It was assumed that an overestimation of the oxygen transferred from the oxygen car rier to methane could be the result of an underestimation of the parameter δ, as set in the numerical simulation. In order to investi gate this point, a 0D study, in which δ was made to vary, was con ducted. Fig. 14a and b show the time evolutions of the solid conversion and oxygen mass transfer rate at 1223 K and 15 %vol. of methane. Measurements from TGA experiments (de Diego et al., 2014) were reported for the purpose of comparison. The results showed that for higher values of δ, lower amounts of oxygen mass transfer rates were obtained, although similar conversions (X_r) were observed, that is, similar oxidation degrees ($X \quad 1 \quad X_r$). The results suggested that accounting for a reduced total oxygen transport capacity would decrease the amount of oxygen trans ferred in FR, thus, improving predictions pertaining to fuel conver sion. A reduced total oxygen transport capacity was suggested by de Diego et al. (2014). The authors identified a loss in the oxygen uncoupling capacity with the redox cycle number in TGA experi ments, which meant that the capability of the perovskite material to transport oxygen was, in fact, decreased in the CLC process.

Numerical results pertaining to instantaneous molar fractions of the major species leaving FR and AR are reported in Fig. 15a and b, respectively. The corresponding time averaged values were also included for comparison with experimental data. Globally, the numerical results matched the experimental measurements in AR considerably well. Predictions in FR were consistent with the observed overestimation of the methane conversion, as previously discussed. Conceming the oxidation process, only one reaction was considered in the modeling, which was the most relevant in the experiments. The results showed that an accurate modeling of such a reaction, combined with an accurate prediction of the solid mass in AR, led to reliable predictions of gaseous species molar fractions. The analysis of gaseous species distribution provided some amount of information pertaining to gas mixing at different locations inside the CLC unit. Local and instantaneous gaseous species molar frac tions at the end of the simulation are shown in Fig. 16. From these results, it was evident that methane and oxygen never came into contact with each other in the system, which was because of the fluidizing steam at the loop seals. This information was critical because it proved the efficiency of the system in capturing CO_2 from exhaust gases of the fuel reactor.

Numerical *versus* experimental results for the gas temperature are shown in Fig. 17a. In the experiments, the temperature probes were located near the reactor wall, 5 to 10 mm into the reactor. Thus, the plots displayed the axial profiles of the time averaged gas temperature in FR and AR, 10 mm from the wall as well. Results showed that numerical predictions did not exactly match the experimental data in both reactors. In the numerical modeling,

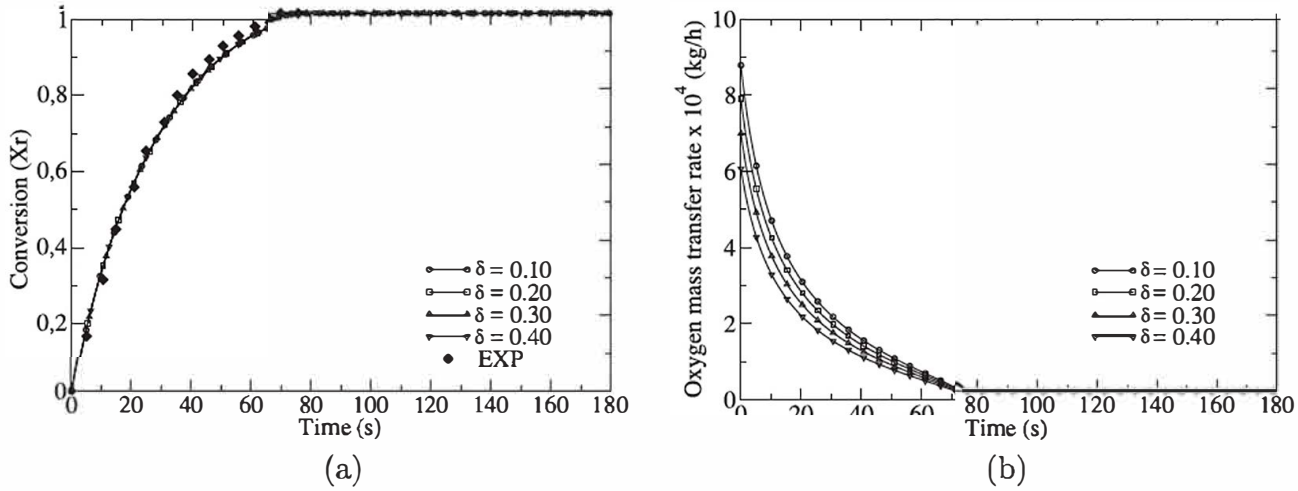

Fig. 14. 0D-model results for (a) solid conversion and (b) oxygen mass transfer rates during reduction at 1223 K and 15 %vol. of methane.

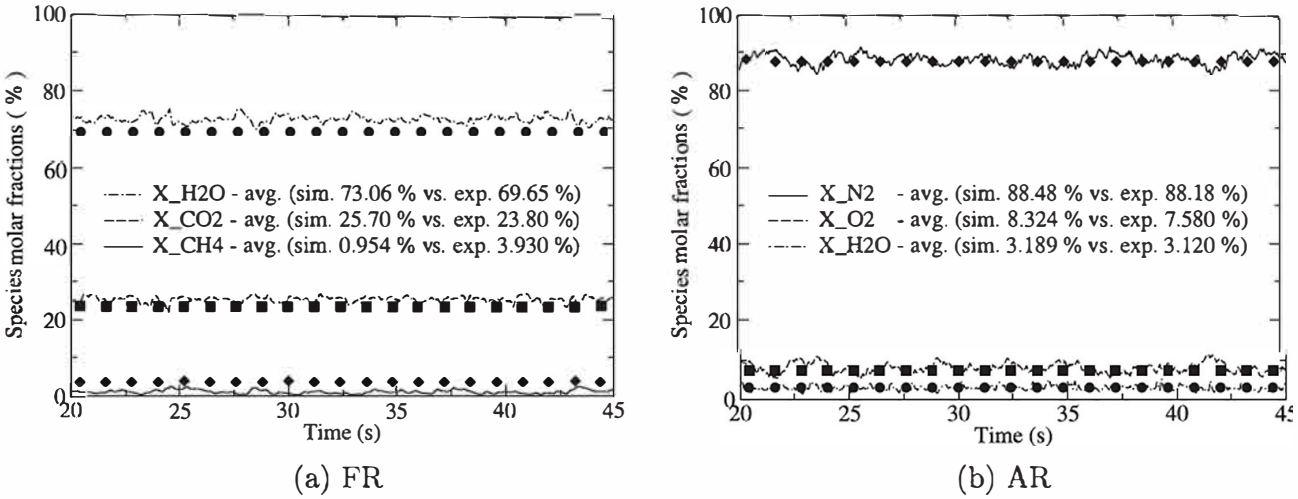

Fig. 15. Instantaneous and mean molar fractions of gaseous species leaving the fuel reactor (experimental results in symbols).

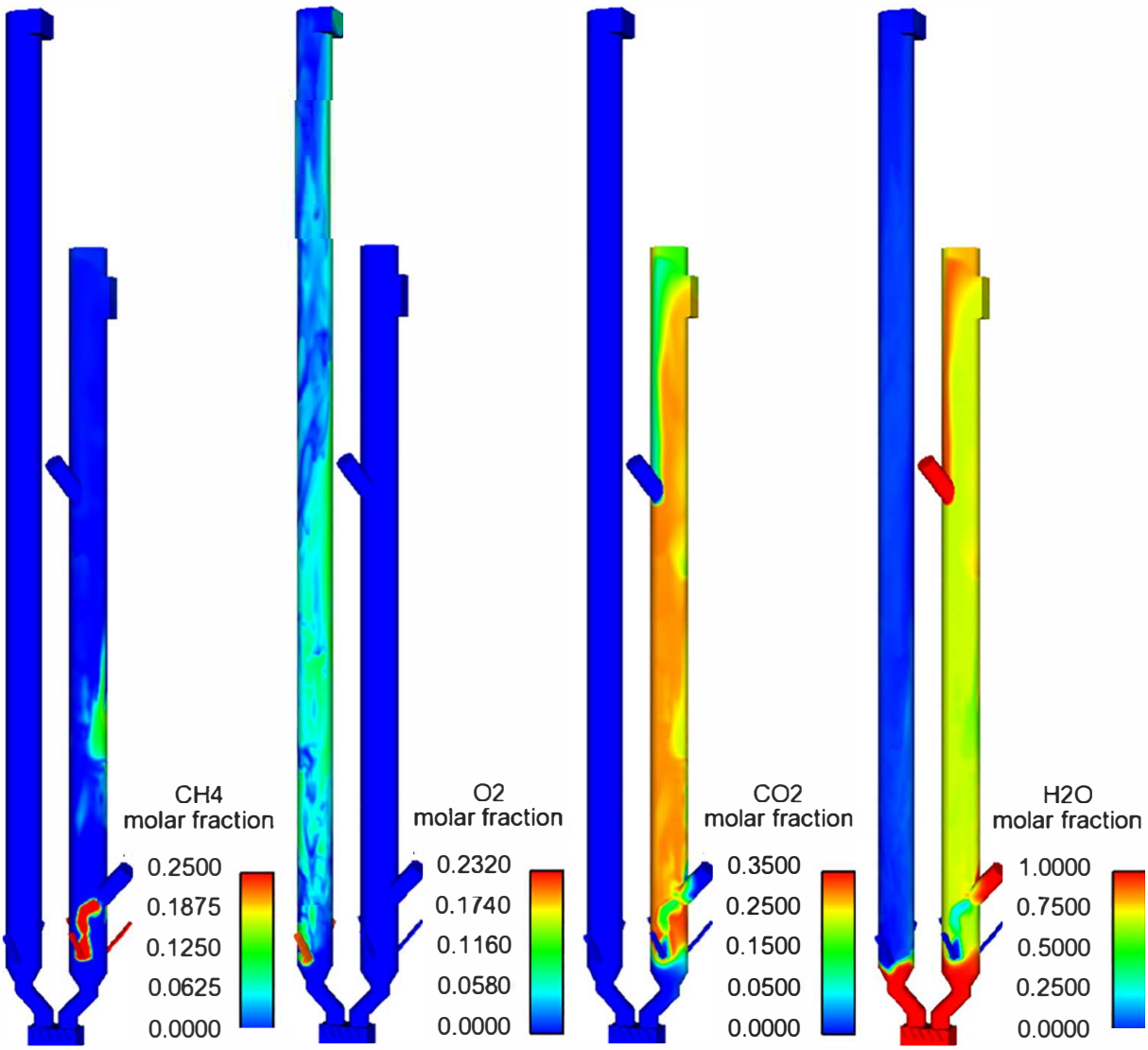

Fig. 16. Local and instantaneous molar fractions of methane, oxygen, carbon dioxide, and water vapor at the end of the simulation.

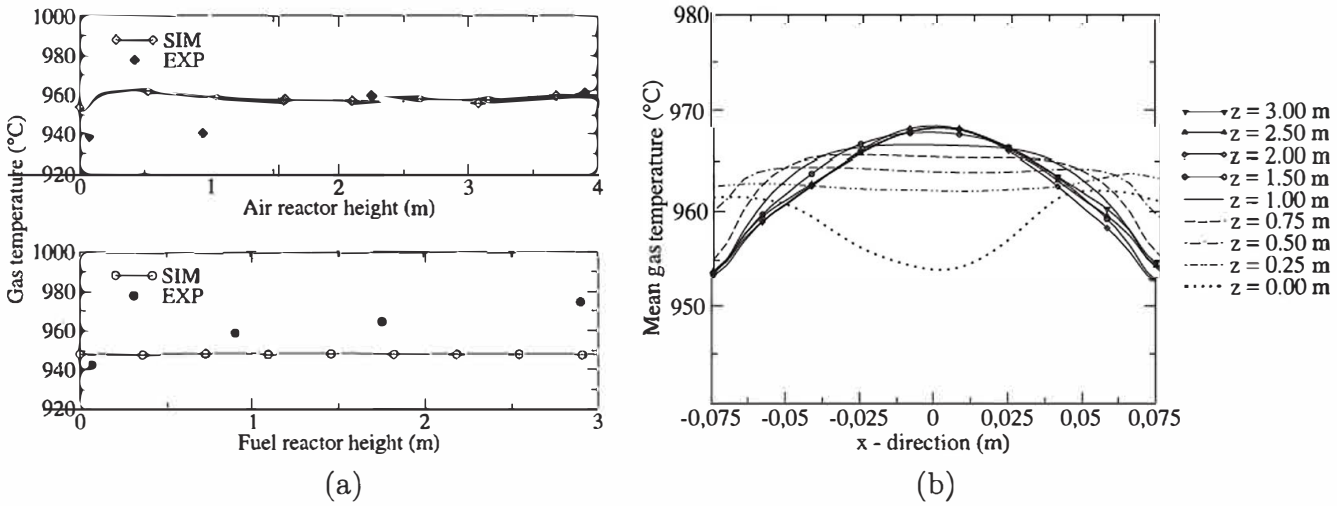

Fig. 17. (a) Numerical against experimental time-averaged gas temperatures along the reactor heights, and (b) radial profiles of the time-averaged gas temperature in AR.

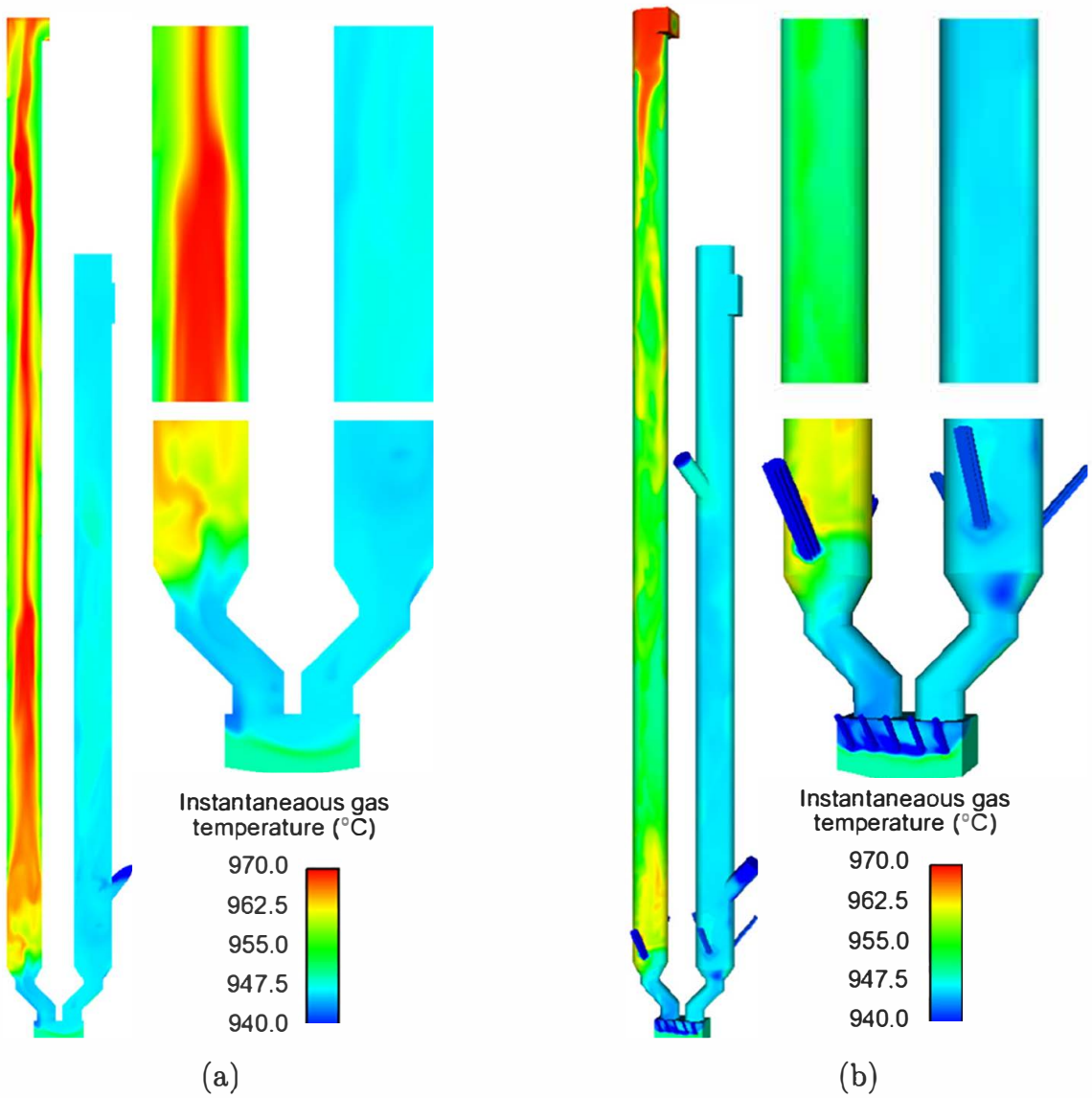

Fig. 18. Local and instantaneous gas temperatures at the end of the simulation: (a) 2D cut, (b) 3D view.

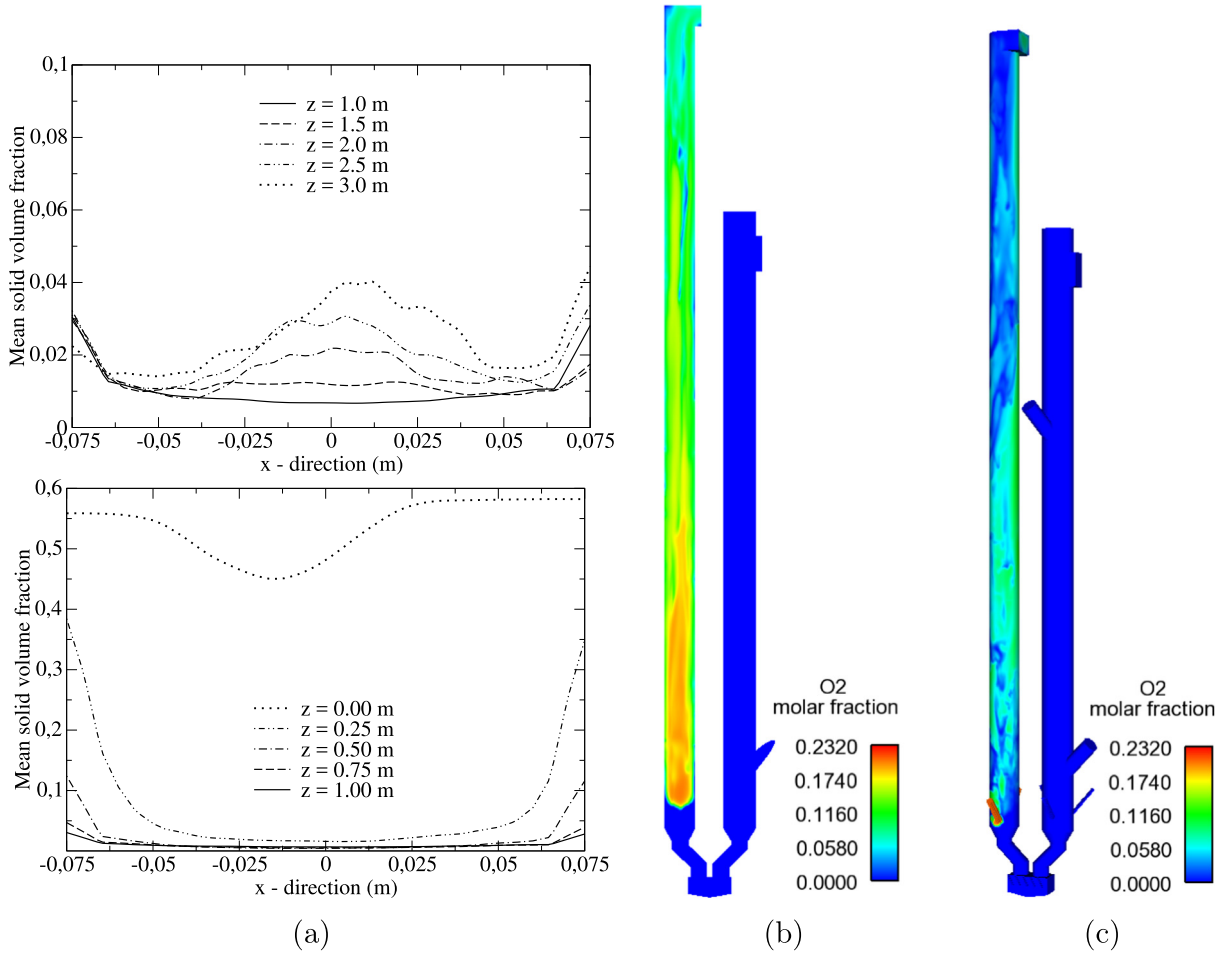

Fig. 19. Radial profiles of the time-averaged solid volume fraction (a) at different locations (z) within the air reactor. Local and instantaneous oxygen molar fraction (b) inside CLC (2D cut), and (c) near the wall.

some assumptions were made to model the standard enthalpy of the reduction and oxidation reactions (Section 3.6). In the numer ical simulation, heat release was attributed to the oxidation reac tion in AR, whereas no heat exchange was accounted for in the reduction reaction in FR. Consequently, it was expected that the mean gas temperature could remain practically constant in FR, whereas it could vary in AR, as observed in Fig. 17a. Concerning FR, it should be noted that in the numerical simulation, activated particles were considered, in which the oxygen uncoupling reac tion was neglected because of its low relevance in the selected OC (de Diego et al., 2014). However, such an OC is a CLOU (Chem ical Looping with Oxygen Uncoupling) material, which can release oxygen in the FR (Mayer et al., 2015). In the experiments, it was assumed that OC coming from AR released a small amount of gas eous oxygen, which reacted with the unconverted methane in FR. This led to a strongly exothermic reaction, which occurred near and below the injection zone, whereas particles fell towards the bed and increased the gas temperature in FR. Because the oxygen uncoupling reaction was neglected in the numerical simulation, this gas temperature increase cannot be reproduced by numerical results. Radial time averaged gas temperature profiles at different AR locations are shown in Fig. 17b. A local and instantaneous view of the gas temperature in CLC is also given in Fig. 18. Results showed that the temperature increased at the AR center because of the oxidation process. Moreover, from the center to the wall, the gas temperature was not uniform. This was because of the thermal boundary conditions imposed at the AR wall. By account ing for a radiative (particle particle, particle wall) heat flux, a more uniform distribution within AR and lower value at the bot tom should result (Konan et al., 2010a; Konan et al., 2010b).

The effect of particle volume fraction on the oxidation reac tion was also analyzed. Time averaged solid volume fractions, at different reactor heights, are shown in Fig. 19a. The local and instantaneous oxygen molar fractions within AR (2D cut) and close to the wall (3D view) at the end of the simulation are depicted in Fig. 19b and c. As expected, a rapid decrease in the particle volume fraction along its axial direction was exhib ited by AR. Moreover, inhomogeneous radial solid volume frac tion profiles were observed. Such inhomogeneities reflected the existence of a stationary core annular distribution of the solid, usually observed in circulating fluidized beds: a dilute core and dense annulus near the reactor wall (for further details, the reader is referred to Rhodes (1990) and references therein). Higher particle concentrations near the wall resulted to a higher oxygen consumption at this location, which explained the lower oxygen molar fractions near the wall than in the reactor center (Fig. 19c *versus* Fig. 19b).

6. Conclusion

In this work, a model based on an Euler Euler approach to com pute both gas and solid phases was developed in order to predict the local and instantaneous behavior of the complex reactive flow inherent in the CLC process. The developed model was used to per form unsteady three dimensional numerical simulations of a CLC unit corresponding to a 120 kW pilot plant working with

perovskite $CaMn_{0.9}Mg_{0.1}O_{3-\delta}$ as oxygen carrier (Mayer et al., 2015). The results obtained from the 3D unsteady numerical simulations were then assessed against experimental measurements over all quantities of interest in the CLC process, which were available from the experiments.

Reduction and oxidation were modeled using the grain model, accounting for the external mass transfer, product layer diffusion, and chemical reaction in the overall chemical reaction process between solid particles and reacting gaseous species. Redox kinetic parameters and reaction mechanisms proposed by de Diego et al. (2014) were used. The heat release was only attributed to the oxi dation reaction, which occurred in the air reactor. Heat exchanges at the air reactor wall were accounted for in the model by using a given wall temperature, as well as separate gas and particle wall heat exchange coefficients, which were written in terms of phase variables at the first interior computational cell. As a first approx imation, radiative heat fluxes were neglected for both phases.

The unsteady three dimensional numerical simulations of the CLC unit were performed using the NEPTUNE_CFD code. The upper and internal loop seals were not accounted for in the numerical configuration, but their effects were reproduced by appropriate boundary conditions. For this reason, two simulations were con ducted in order to estimate the total solid inventory without the discarded zones. The system was loaded with an amount of (par tially oxidized) solid mass corresponding to a quantity a priori esti mated on the basis of particle properties, and physical and geometric considerations. The numerical simulation, using a 30 kg solid inventory, was found to correctly predict the solid mass reported by experiments in each reactor; this simulation was therefore retained for the purpose of analysis.

The results showed the ability of the Euler Euler approach to accurately predict the entire CLC behavior. The existence of a core annular flow structure in the dilute regions of the air reactor and the bubbling behavior in the fuel reactor were reproduced by numerical simulations. A good agreement was found between the numerical and experimental results pertaining to the gas pressure drop, the solid mass distribution within the system, and the global solid circulation between reactors. Thermodynamics and reactions were also investigated, and the results were compared with exper imental data. The extents of oxidation at the top of the air reactor and in the lower loop seal agreed considerably well with experi mental measurements. The predictions of gaseous species molar fractions in the air reactor were also found considerably satisfac tory. On the other hand, in the fuel reactor, an underestimation of the methane molar fraction was observed. Such an underestima tion corresponded to an overestimation of the fuel conversion at the fuel reactor outlet. The difference between the numerical results and experimental measurements was attributed to the per ovskite formula retained in this study, which was related to the model of the oxygen transport capacity at the selected operating point (temperature and oxygen partial pressure). According to de Diego et al. (2014) the total oxygen transport capacity of the per ovskite material should decrease in the CLC when particles are activated. Therefore, a reduced total oxygen transport capacity should be taken into account in the modeling. Concerning the gas temperature, numerical results were found to slightly differ from experimental measurements. However, such a difference was small, and predictions could be improved using more accurate values of heat release for each reaction, together with more sophis ticated models for heat exchange at the wall, thermal radiation between phases, and between each phase and the wall in the air reactor. Finally, the results identified a considerably long transient regime, which was attributed to characteristic time scales inherent in the CLC process. However, the convergence of results was extre mely slow; an aspect that deserves further investigations and left as a future work.

Acknowledgements

This work received funding from the European Community through the SUCCESS project under the 7th Framework program (Grant agreement No. 608571). It reflects only the author's views, and the Community is not liable for any use that may be made of the information contained herein. This work was granted access to the HPC resources of CALMIP supercomputing center under allo cation 2016 0111 and of CINES supercomputing center under allo cation A0022B06012. Accordingly, CALMIP and CINES are gratefully acknowledged. The authors would like to thank Prof. Juan Adánez for productive discussions and Ing. Hervé Neau for the numerical support with the NEPTUNE_CFD code.

References

Abad, A., Mattisson, T., Lyngfelt, A., Johansson, M., 2007. The use of iron oxide as oxygen carrier in a chemical-looping reactor. Fuel 86 (7), 1021–1035.
Abad, A., Adánez, J., García-Labiano, F., de Diego, L.F., Gayán, P., 2010. Modeling of the chemical-looping combustion of methane using a Cu-based oxygen-carrier. Combust. Flame 157 (3), 602–615.
Abad, A., Gayán, P., de Diego, L.F., García-Labiano, F., Adánez, J., 2013. Fuel reactor modelling in chemical-looping combustion of coal: 1. model formulation. Chem. Eng. Sci. 87, 277–293.
Abad, A., Gayán, P., de Diego, L.F., García-Labiano, F., Adánez, J., Mayer, K., Penthor, S., 2014. Modelling a CLC process improved by CLOU and validation in a 120 kW unit. In: Proceedings of the 11th International Conference on Fluidized Bed Technology, CFB-11, pp. 861–867.
Abad, A., Gayán, P., García-Labiano, F., de Diego, L.F., Adánez, J., 2018. Relevance of plant design on CLC process performance using a Cu-based oxygen carrier. Fuel Process. Technol. 171, 78–88.
Alobaid, F., Ohlemüller, P., Ströhle, J., Epple, B., 2015. Extended Euler-Euler model for the simulation of a 1 MWth chemical-looping pilot plant. Energy 93 (Part 2), 2395–2405.
Bakken, E., Norby, T., Stølen, S., 2005. Nonstoichiometry and reductive decomposition of $CaMnO_{3-\delta}$. Solid State Ionics 176 (1-2), 217–223.
Banerjee, S., Agarwal, R.K., 2015. An Eulerian approach to computational fluid dynamics simulation of a chemical-looping combustion reactor with chemical reactions. J. Energy Res. Technol. 138 (4), 042201–042201–9.
Bird, R.B., Stewart, W.E., Lightfoot, E.N., 2007. Transport Phenomena. John Wiley & Sons.
Boëlle, A., Balzer, G., Simonin, O., 1995. Second-order prediction of the particle-phase stress tensor of inelastic spheres in simple shear dense suspensions. Gas-Solid flows, ASME FED 228, 9–18.
Bolhàr-Nordenkampf, J., Pröll, T., Kolbitsch, P., Hofbauer, H., 2009. Comprehensive modeling tool for chemical looping based processes. Chem. Eng. Technol. 32 (3), 410–417.
Cabello, A., Abad, A., García-Labiano, F., Gayán, P., de Diego, L.F., Adánez, J., 2014. Kinetic determination of a highly reactive impregnated Fe_2O_3/Al_2O_3 oxygen carrier for use in gas-fueled Chemical Looping Combustion. Chem. Eng. J. 258, 265–280.
Cabello, A., Gayán, P., García-Labiano, F., de Diego, L.F., Abad, A., Adánez, J., 2016a. On the attrition evaluation of oxygen carriers in Chemical Looping Combustion. Fuel Process. Technol. 148, 188–197.
Cabello, A., Gayán, P., Abad, A., de Diego, L.F., García-Labiano, F., Izquierdo, M.T., Scullard, A., Williams, G., Adánez, J., 2016b. Long-lasting Cu-based oxygen carrier material for industrial scale in Chemical Looping Combustion. Int. J. Greenhouse Gas Control 52, 120–129.
Chen, L., Yang, X., Li, G., Li, X., Snape, C., 2017. Prediction of bubble fluidisation during chemical looping combustion using CFD simulation. Comput. Chem. Eng. 99, 82–95.
de Diego, L.F., Abad, A., Cabello, A., Gayán, P., García-Labiano, F., Adánez, J., 2014. Reduction and oxidation kinetics of a $CaMn_{0.9}Mg_{0.1}O_{3-\delta}$ oxygen carrier for chemical-looping combustion. Ind. Eng. Chem. Res. 53 (1), 87–103.
Deng, Z., Xiao, R., Jin, B., Song, Q., Huang, H., 2008. Multiphase CFD modeling for a chemical looping combustion process (fuel reactor). Chem. Eng. Technol. 31 (12), 1754–1766.
Fede, P., Simonin, O., Ingram, A., 2016. 3D numerical simulation of a lab-scale pressurized dense fluidized bed focussing on the effect of the particle-particle restitution coefficient and particle–wall boundary conditions. Chem. Eng. Sci. 142, 215–235.
Frössling, N., 1938. Über die verdunstung fallender tropfen. Gerlands Beitr. Geophys 52, 170–216.
García-Labiano, F., de Diego, L.F., Gayán, P., Abad, A., Adánez, J., 2013. Fuel reactor modelling in chemical-looping combustion of coal: 2–simulation and optimization. Chem. Eng. Sci. 87, 173–182.
Gauthier, T., Yazdanpanah, M., Forret, A., Amblard, B., Lambert, A., Bertholin, S., 2017. CLC, a promising concept with challenging development issues. Powder Technol. 316, 3–17.
Geng, C., Zhong, W., Shao, Y., Chen, D., Jin, B., 2015. Computational study of solid circulation in chemical-looping combustion reactor model. Powder Technol. 276, 144–155.

Gobin, A., Neau, H., Simonin, O., Llinas, J.-R., Reiling, V., Sélo, J.-L., 2003. Fluid dynamic numerical simulation of a gas phase polymerization reactor. Int. J. Numer. Meth. Fluids 43 (10-11), 1199–1220.

Guan, Y., Chang, J., Zhang, K., Wang, B., Sun, Q., 2014. Three-dimensional CFD simulation of hydrodynamics in an interconnected fluidized bed for chemical looping combustion. Powder Technol. 268, 316–328.

Guan, Y., Chang, J., Zhang, K., Wang, B., Sun, Q., Wen, D., 2016. Three-dimensional full loop simulation of solids circulation in an interconnected fluidized bed. Powder Technol. 289, 118–125.

Hallberg, P., Rydén, M., Mattisson, T., Lyngfelt, A., 2014. $CaMnO_{3-\delta}$ made from low cost material examined as oxygen carrier in chemical-looping combustion. Energy Procedia 63, 80–86.

Hamidouche, Z., 2017. Modeling and numerical simulation of coupled reactive fluidized beds in a chemical looping combustion system, Ph.D. thesis, Intitut National Polytechnique de Toulouse, France. URL http://oatao.univ-toulouse.fr/.

Hamidouche, Z., Masi, E., Fede, P., Ansart, R., Neau, H., Hemati, M., Simonin, O., 2018. Chapter two – numerical simulation of multiphase reactive flows. In: Parente, A., Wilde, J.D. (Eds.), Bridging Scales in Modelling and Simulation of Non-Reacting and Reacting Flows. Part I, Vol. 52 of Advances in Chemical Engineering. Academic Press, pp. 51–124.

Haus, J., Hartge, E.-U., Heinrich, S., Werther, J., 2017. Dynamic flowsheet simulation of gas and solids flows in a system of coupled fluidized bed reactors for chemical looping combustion. Powder Technol. 316, 628–640.

Igci, Y., Andrews, A.T., Sundaresan, S., Pannala, S., O'Brien, T., 2008. Filtered two-fluid models for fluidized gas-particle suspensions. AIChE J. 54 (6), 1431–1448.

Igci, Y., Pannala, S., Benyahia, S., Sundaresan, S., 2012. Validation studies on filtered model equations for gas-particle flows in risers. Ind. Eng. Chem. Res. 51 (4), 2094–2103.

Jing, D., Jacobs, M., Hallberg, P., Lyngfelt, A., Mattisson, T., 2016. Development of $CaMn_{0.775}Mg_{0.1}Ti_{0.125}O_{3-\delta}$ oxygen carriers produced from different Mn and Ti sources. Mater. Des. 89, 527–542.

Johansson, E., Lyngfelt, A., Mattisson, T., Johnsson, F., 2003. Gas leakage measurements in a cold model of an interconnected fluidized bed for chemical-looping combustion. Powder Technol. 134 (3), 210–217.

Jung, J., Gamwo, I.K., 2008. Multiphase CFD-based models for chemical looping combustion process: Fuel reactor modeling. Powder Technol. 183 (3), 401–409.

Kolbitsch, P., Pröll, T., Bolhar-Nordenkampf, J., Hofbauer, H., 2009a. Design of a chemical looping combustor using a dual circulating fluidized bed (DCFB) reactor system. Chem. Eng. Technol. 32 (3), 398–403.

Kolbitsch, P., Pröll, T., Bolhar-Nordenkampf, J., Hofbauer, H., 2009b. Characterization of chemical looping pilot plant performance via experimental determination of solids conversion. Energy Fuels 23 (3), 1450–1455.

Konan, N., Neau, H., Simonin, O., Dupoizat, M., Le Goaziou, T., 2010a. 3D unsteady multiphase simulation of uranium tetrafluoride particle fluorination in fluidized bed pilot. In: Yue, Guangxi, Zhang, Hai, Zhao, Changsui, Luo, Zhongyang (Eds.), Proceedings of the 20th International Conference on Fluidized Bed Combustion. Springer Berlin Heidelberg, pp. 1152–1158.

Konan, N., Neau, H., Simonin, O., Dupoizat, M., Le Goaziou, T., 2010b. Reactive multiphase flow simulation of uranium hexafluoride conversion reactor. In: Proceedings of the 7th International Conference on Multiphase Flow, Tampa, FL, May 30-June 4, 2010.

Kruggel-Emden, H., Rickelt, S., Stepanek, F., Munjiza, A., 2010. Development and testing of an interconnected multiphase CFD-model for chemical looping combustion. Chem. Eng. Sci. 65 (16), 4732–4745.

Leonidova, E.I., Leonidov, I.A., Patrakeev, M.V., Kozhevnikov, V.L., 2011. Oxygen non-stoichiometry, high-temperature properties, and phase diagram of $CaMnO_{3-\delta}$. J. Solid State Electrochem. 15 (5), 1071–1075.

Mahalatkar, K., Kuhlman, J., Huckaby, E.D., O'Brien, T., 2011a. CFD simulation of a chemical-looping fuel reactor utilizing solid fuel. Chem. Eng. Sci. 66 (16), 3617–3627.

Mahalatkar, K., Kuhlman, J., Huckaby, E.D., O'Brien, T., 2011b. Simulations of a circulating fluidized bed chemical looping combustion system utilizing gaseous fuel. Oil Gas Sci. Technol. – Rev. IFP Energies Nouvelles 66 (2), 301–311.

Markström, P., Lyngfelt, A., 2012. Designing and operating a cold-flow model of a 100kW chemical-looping combustor. Powder Technol. 222, 182–192.

Marx, K., Bertsch, O., Pröll, T., Hofbauer, H., 2013. Next scale chemical looping combustion: process integration and part load investigations for a 10MW demonstration unit. Energy Procedia 37, 635–644.

Mayer, K., Penthor, S., Pröll, T., Hofbauer, H., 2015. The different demands of oxygen carriers on the reactor system of a CLC plant – Results of oxygen carrier testing in a 120 kW_{th} pilot plant. Appl. Energy 157, 323–329.

Neau, H., Fede, P., Laviéville, J., Simonin, O., 2013. High Performance Computing (HPC) for the fluidization of particle-laden reactive flows. In: Proceedings of the 14th International Conference on Fluidization-From Fundamentals to Products, Eds, ECI Symposium Series.

Ohlemüller, P., Alobaid, F., Gunnarsson, A., Ströhle, J., Epple, B., 2015. Development of a process model for coal chemical looping combustion and validation against 100kWth tests. Appl. Energy 157, 433–448.

Özel, A., Fede, P., Simonin, O., 2013. Development of filtered Euler–Euler two-phase model for circulating fluidised bed: high resolution simulation, formulation and a *priori* analyses. Int. J. Multiph. Flow 55, 43–63.

Parker, J.M., 2014. CFD model for the simulation of chemical looping combustion. Powder Technol. 265, 47–53.

Parmentier, J.-F., Simonin, O., Delsart, O., 2012. A functional subgrid drift velocity model for filtered drag prediction in dense fluidized bed. AIChE J. 58 (4), 1084–1098.

Penthor, S., Zerobin, F., Mayer, K., Pröll, T., Hofbauer, H., 2015. Investigation of the performance of a copper based oxygen carrier for chemical looping combustion in a 120kW pilot plant for gaseous fuels. Appl. Energy 145, 52–59.

Penthor, S., Stollhof, M., Pröll, T., Hofbauer, H., 2016. Detailed fluid dynamic investigations of a novel fuel reactor concept for chemical looping combustion of solid fuels. Powder Technol. 287, 61–69.

Penthor, S., Mattisson, T., Adánez, J., Bertolin, S., Masi, E., Larring, Y., Langørgen, Øyvind, Ströhle, J., Snijkers, F., Geerts, L., Albertsen, K., Williams, G., Bertsch, O., Authier, O., Dávila, Y., Yazdanpanah, M., Pröll, T., Lyngfelt, A., Hofbauer, H., 2017. The EU-FP7 Project SUCCESS - Scale-up of Oxygen Carrier for Chemical Looping Combustion using Environmentally Sustainable Materials. Energy Procedia 114, 395–406.

Pishahang, M., Larring, Y., Sunding, M., Jacobs, M., Snijkers, F., 2016. Performance of perovskite-type oxides as oxygen-carrier materials for chemical looping combustion in the presence of H2S. Energy Technol. 4 (10), 1305–1316.

Pröll, T., Kolbitsch, P., Bolhàr-Nordenkampf, J., Hofbauer, H., 2009a. A novel dual circulating fluidized bed system for chemical looping processes. AIChE J. 55 (12), 3255–3266.

Pröll, T., Rupanovits, K., Kolbitsch, P., Bolhàr-Nordenkampf, J., Hofbauer, H., 2009b. Cold flow model study on a dual circulating fluidized bed (DCFB) system for chemical looping processes. Chem. Eng. Technol. 32 (3), 418–424.

Rhodes, M.J., 1990. Modelling the flow structure of upward-flowing gas-solids suspensions. Powder Technol. 60 (1), 27–38.

Schneiderbauer, S., 2017. A spatially-averaged two-fluid model for dense large-scale gas-solid flows. AIChE J. 63 (8), 3544–3562.

Sharma, R., May, J., Alobaid, F., Ohlemüller, P., Ströhle, J., Epple, B., 2017. Euler-Euler CFD simulation of the fuel reactor of a 1MWth chemical-looping pilot plant: Influence of the drag models and specularity coefficient. Fuel 200, 435–446.

Simonin, O., 2000. Statistical and continuum modelling of turbulent reactive particulate flows. Part 1: Theoretical derivation of dispersed Eulerian modelling from probability density function kinetic equation. In: Lecture Series, Vol. 6, In book: Theoretical and Experimental Modeling of Particulate Flows. von Karman Institute for Fluid Dynamics, Rhode Saint Genèse, Belgium.

Su, M., Zhao, H., Ma, J., 2015. Computational fluid dynamics simulation for chemical looping combustion of coal in a dual circulation fluidized bed. Energy Convers. Manage. 105, 1–12.

Vermorel, O., Bédat, B., Simonin, O., Poinsot, T., 2003. Numerical study and modelling of turbulence modulation in a particle laden slab flow. J. Turbul. 4, N25.

Wang, S., Lu, H., Zhao, F., Liu, G., 2014. CFD studies of dual circulating fluidized bed reactors for chemical looping combustion processes. Chem. Eng. J. 236, 121–130.

Web site of the NIST Chemistry WebBook, http://webbook.nist.gov/chemistry/.

Zerobin, F., Bertsch, O., Penthor, S., Pröll, T., 2016. Concept study for competitive power generation from chemical looping combustion of natural gas. Energy Technol. 4 (10), 1299–1304.

Zerobin, F., Penthor, S., Bertsch, O., Pröll, T., 2017. Fluidized bed reactor design study for pressurized chemical looping combustion of natural gas. Powder Technol. 316, 569–577.

Zhang, Y., Chao, Z., Jakobsen, H.A., 2017. Modelling and simulation of chemical looping combustion process in a double loop circulating fluidized bed reactor. Chem. Eng. J. 320, 271–282.